American Mineralogist, Volume 65, pages 225–271, 1980

The melting relations at 1 bar of pyroxenes composed largely of Ca-, Mg-, and Fe-bearing components

J. STEPHEN HUEBNER

U.S. Geological Survey
Reston, Virginia 22092

AND ALLEN C. TURNOCK

Department of Earth Sciences, University of Manitoba
Winnipeg, Canada R3T 2N2

Abstract

Temperature–composition sections were constructed from the results of quenching experiments (1 bar pressure; oxygen fugacity values close to those of the assemblage iron–wüstite) using bulk compositions in the pyroxene quadrilateral composition plane, $Mg_2Si_2O_6$–$CaMgSi_2O_6$–$CaFeSi_2O_6$–$Fe_2Si_2O_6$. The new results were combined with previously published phase equilibrium data for metasilicate compositions in the pure system MgO–CaO–FeO–SiO_2 to derive a comprehensive phase diagram for bulk compositions that lie in the pyroxene plane. Orthopyroxene and augite cannot coexist in this four-component system because, in the presence of melt, the pigeonite field separates the augite and orthopyroxene fields on both the solidus and the liquidus surfaces.

Single crystals of lunar and terrestrial pyroxenes, which lie close to the pyroxene composition plane but contain minor amounts of Al, Ti, Cr, and Mn, were heated under similar conditions. On partial melting, Al and Ti are partitioned into the liquid, diluting it in the major pyroxene components, thereby lowering the range of solidus (and liquidus) temperatures. At the reduced solidus temperatures of the natural pyroxene system, both orthopyroxene + augite and pigeonite + augite are stable assemblages. The phase diagram for natural pyroxene compositions, presented as a series of isothermal sections, is potentially useful for understanding pyroxene–melt relationships during magmatic crystallization or fractional melting at low pressure.

I. Introduction

Most rock-forming pyroxenes have compositions that plot on or near to the pyroxene quadrilateral plane $Mg_2Si_2O_6$–$CaMgSi_2O_6$–$CaFeSi_2O_6$–$Fe_2Si_2O_6$ (En–Di–Hd–Fs) in the system CaO–MgO–FeO–SiO_2 (Fig. 1). However, there have been few experimental investigations of the phase relations of pyroxene bulk compositions that lie other than at the sides of the pyroxene composition plane, probably because of the time-consuming nature of such a study and experimental difficulties in proper phase characterization. Much of the information bearing on low-pressure pyroxene phase relations has been gleaned from observations of coexisting natural pyroxenes and pyroxene fractionation trends in basaltic rocks (Kuno, 1966; Dallwitz *et al.*, 1966; Nakamura, 1971).

The application of earlier experimental investigations of simple synthetic systems to the interpretation of the crystallization of natural pyroxenes and pyroxene-bearing rocks has not been successful. Two problems could not be investigated in this manner: the nature of the pigeonite stability field, which lies within the quadrilateral under most geological conditions; and the effect of changing the bulk composition of the system to approximate better the compositions of real pyroxenes, magmas, and rocks.

A recent revival of interest in pyroxenes, stimulated in part by the abundance of pyroxenes in lunar samples, has increased the knowledge of pyroxene mineralogy and has motivated several experimental studies of pyroxene phase relations. Integration of the new results with the old and application of the pyroxene data to rock genesis have been hindered by

0003–004X/80/0304–0225$02.00

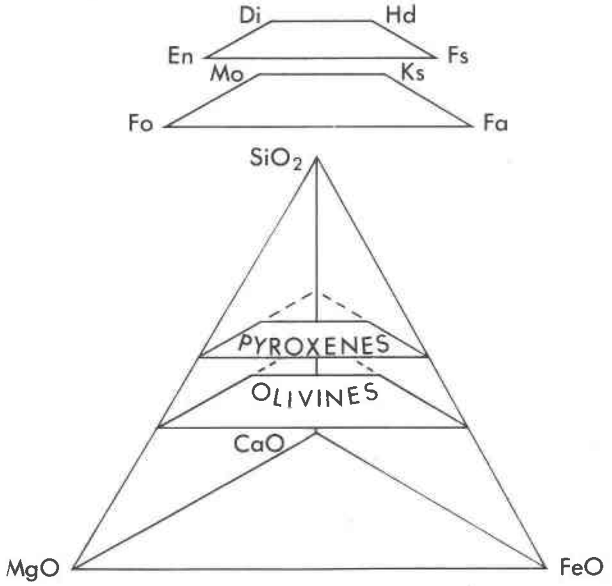

Fig. 1. Composition tetrahedron for the pure system CaO–MgO–FeO–SiO_2 showing component compositions, and the positions of the metasilicate (En–Di–Hd–Fs) and orthosilicate (Fo–Mo–Ks–Fa) quadrilateral planes. Abbreviations: En, enstatite ($Mg_2Si_2O_6$); Di, diopside ($CaMgSi_2O_6$); Hd, hedenbergite ($CaFeSi_2O_6$); Fs, ferrosilite ($Fe_2Si_2O_6$); Fo, forsterite (Mg_2SiO_4); Fa, fayalite (Fe_2SiO_4); Mo, monticellite ($CaMgSiO_4$); and Ks, kirschsteinite ($CaFeSiO_4$).

the lack of comprehensive phase diagrams both for pyroxene bulk compositions and for pyroxene assemblages in real rocks. The purpose of this paper is to provide such diagrams for pyroxenes by drawing upon our experimental data and those of other investigators.

The topology of these diagrams will provide a framework with which to interpret natural assemblages and experimental run products. To the extent that the fields of these diagrams are accurately placed in temperature–composition space, the diagrams will be useful in planning further experimentation, particularly determinations of trace-element partitioning between pyroxene crystals and melt.

Crystal chemistry of phases

The following nomenclature has been adopted for the phases that have compositions close to the pyroxene quadrilateral. Augite (A) is a calcium-rich pyroxene with space group *C2/c*; the Wo content [mole % $CaSiO_3$, 100 Ca/(Ca+Mg+Fe)] exceeds 20% and may be as great as 50% (as in the diopside–hedenbergite solid-solution series). Orthopyroxene (O) is orthorhombic (*Pbca*) with Wo < 7. Pigeonite (P) is a calcium-poor clinopyroxene ($P2_1/c$ at low temperature, *C2/c* symmetry at high temperature; Prewitt *et al.*, 1971) with Wo < 20. The calcium-poor pyroxenes called clinoenstatite and clinohypersthene by many investigators are isostructural with pigeonite and are not treated as distinct mineral phases in this paper. Protoenstatite, an enigmatic enstatite polymorph at compositions near $MgSiO_3$, is of little importance to terrestrial or lunar rocks; we have chosen to ignore this phase by merging its stability field into that of orthopyroxene. A pyroxenoid, ferrobustamite solid solution (Rapoport and Burnham, 1973) (B) is the high-temperature polymorph of iron-rich augite (ferroaugite or hedenbergite). Under some conditions encountered in this study, phases were present which did not have compositions close to the quadrilateral. They include olivine (F), Mg_2SiO_4–Fe_2SiO_4 solid solution; silica (S, tridymite, cristobalite); and melt (designated L). At 1 bar pressure, the pyroxene systems are condensed; "pyroxene" vapor is negligible and is not considered.

Components

The synthetic phases, here called "pure" phases, contain the four components MgO, CaO, FeO, and SiO_2. With the exception of diopside at temperatures near its liquidus (Kushiro, 1972), pure pyroxene at low pressure neither dissolves excess amounts of oxides such as MgO or SiO_2 nor, at the reducing conditions of the experiments reported herein, contains appreciable Fe^{3+}; these pure pyroxenes plot on the ternary plane $Mg_2Si_2O_6$(En)–$Ca_2Si_2O_6$(Wo)–$Fe_2Si_2O_6$(FS) (Fig. 1). In natural environments, pyroxene compositions depart from this plane and the system MgO–FeO–CaO–SiO_2 toward other components such as Al_2O_3 and TiO_2. In contrast with the "pure" synthetic pyroxenes, we call the natural pyroxenes and pyroxene systems "impure."

For certain pyroxene bulk compositions and temperatures, solids (olivine, silica) and melt that do not plot on the pyroxene composition plane are present (Fig. 1). However, the bulk composition is constrained to the pyroxene plane (in the pure synthetic system) or close to the quadrilateral plane (in impure systems). Olivine and melt compositions are projected from SiO_2 onto solidus diagrams and isothermal sections.

Some discussions have been simplified by the use of "compound" components which are formed by combining the elementary components CaO–MgO–FeO–SiO_2 in various proportions. The pyroxene plane can be described by three components, En–Wo–Fs ($Mg_2Si_2O_6$–$Ca_2Si_2O_6$–$Fe_2Si_2O_6$) or four (coplanar) components En–Di–Hd–Fs ($Mg_2Si_2O_6$–$CaMgSi_2O_6$–$CaFeSi_2O_6$–$Fe_2Si_2O_6$). Similarly, the olivine plane can be described by using compound components Fo–Mo–Ks–Fa (Mg_2SiO_4–$CaMgSiO_4$–$CaFeSiO_4$–Fe_2SiO_4).

Previous work, pure system

Virtually all the available experimental data on pyroxene phase relations at low pressure pertain to the systems bounding the quadrilateral plane and the MgO–CaO–FeO–SiO_2 tetrahedron. Previously published data on the pyroxene quadrilateral at 1 bar pressure are summarized in Figure 2a (liquidus) and Figure 2b (solidus). This early work demonstrates clearly that incongruency is important to understanding pyroxene phase relations; even the simplest pyroxene end-members melt incongruently.

Boyd and Schairer (1964) described the basic relations for the system En–Di at 1 atm pressure. Recently, Yang and Foster (1972), Kushiro (1972), and Yang (1973) reported the existence of an iron-free pigeonite field, shown in Figure 2b. Foster and Lin (1975) and Longhi and Boudreau (1979) advocate the presence of orthopyroxene on the solidus; Ross and Huebner (1979) reason that the protopyroxene reported by Yang (1973) is orthopyroxene, not protopyroxene. Pure $CaMgSi_2O_6$ melts incongruently to a solid solution of Di–En–Fo and a liquid solution of Di–Wo–SiO_2 (Kushiro, 1972).

The join Di–Hd was first described by Turnock (1962) (Fig. 2b). Augite is the liquidus phase for compositions more magnesian than about 100Mg/(Mg+Fe) = 24; "wollastonite" for more hedenbergitic bulk compositions. (The phase "wollastonite" as used by Turnock is the ferrobustamite of Rapoport and Burnham, 1973.) The join Di–Hd is not binary when liquid coexists with this pyroxenoid (Turnock, 1962; Yoder *et al.*, 1964): the pyroxenoid contains more than 50 mole % $CaSiO_3$ and the liquid is correspondingly enriched in $MgSiO_3$ + $FeSiO_3$. At low temperatures there is a continuous augite solid solution from Di to Hd, a result also found at 1 kbar water pressure by Rutstein and Yund (1969) and by Nolan (1969). The $CaFeSi_2O_6$ pyroxene hedenbergite reacts to the pyroxenoid bustamite on heating; except at the composition $CaFeSi_2O_6$, which inverts at a sharply defined temperature, there is a miscibility gap (reaction temperature interval) between hedenbergite and pyroxenoid (see Fig. 2b).

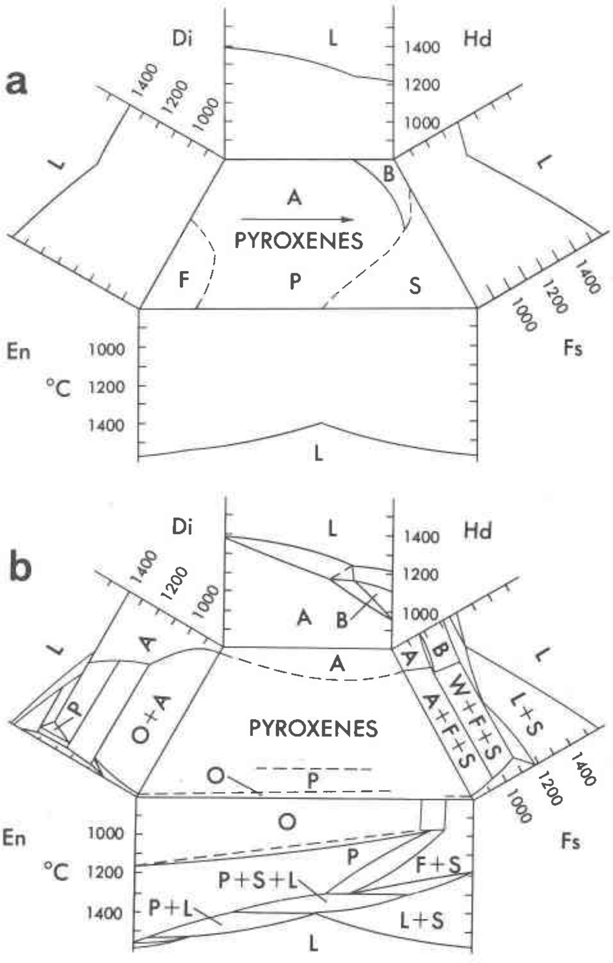

Fig. 2. Unfolded *T–X* prisms showing phase relations determined by previous investigators (see text) for pyroxene quadrilateral bulk compositions in the pure system CaO–MgO–FeO–SiO_2. A = augite; O = orthopyroxene; P = pigeonite; F = olivine; S = silica; B = pyroxenoid, ferrobustamite; L = liquid. Fig. 2a shows the liquidus surface and is based on the bounding systems and the work of Roedder (1965). Fig. 2b is similar to Fig. 2a but emphasizes the sub-liquidus phase relations. The dashed lines delimit, in a generalized manner, the fields of orthopyroxene, pigeonite, and augite in the subsolidus. Temperatures are in °C.

Bowen *et al.* (1933) and Lindsley and Munoz (1969) described the Hd–Fs system. For hedenbergite-rich compositions, augite (or its pyroxenoid inversion product) is the stable subsolidus phase. Hedenbergitic pyroxene cannot contain greater than approximately 60 mole percent Fs in Wo–Fs solid solution at low pressure; with increasing Fs content the one-phase field hedenbergite (A) passes into the three-phase assemblage A+F+S (Fig. 2b). Similarly, at higher temperatures (>~960°C) B and B+F+S are the stable one- and three-phase assemblages, respectively. Melting relations of the join Hd–Fs are complicated by the presence of silica on the liquidus and by pyroxenoid solid solutions richer in $CaSiO_3$ than $CaFeSi_2O_6$ (Bowen *et al.*, 1933). Even if we neglect the presence of ferric iron, melting relations must be considered in terms of Ca_2SiO_4–Fe_2SiO_4–SiO_2.

Subsolidus relations of the composition $MgSiO_3$ have received much attention from experimental mineralogists because of the transformation of orthopyroxene to protopyroxene on heating at temperatures exceeding 1100°C, and the subsequent "inversion" to pigeonite on cooling to room temperature [Smith (1969) and Schwab (1969) reviewed the literature on $MgSiO_3$]. Bowen and Schairer (1935) determined the incongruent melting relations of pure $MgSiO_3$ and investigated the melting relations across the entire En–Fs join. The subsolidus phase relations for the "pure" En–Fs join have not been systematically investigated. Both Bowen and Schairer (1935) and Ross and Huebner (1979) used natural crystals that contain small amounts of calcium (Wo ≤ 4) to study the reaction of orthopyroxene to produce pigeonite and to model the phase relations in the calcium-free system.

Few attempts have been made to investigate the phase relations of compositions lying within (the plane of) the pure pyroxene quadrilateral. Roedder (1965) in 1951 performed a reconnaissance investigation of the liquidus surface (Fig. 2a). He did not distinguish between the Ca-rich and Ca-poor clinopyroxenes (A,P). Neither did he outline a liquidus field of pyroxenoid, although he noted that one composition may have crystallized pyroxenoid coexisting with pyroxene. Turnock (1970), in a preliminary description of the quadrilateral, described a central liquidus field of clinopyroxene which is divided, at least at 1 bar pressure, into fields of augite and pigeonite by a thermal trough at Wo_{33}, descending in temperature as Fe/Mg increases. From this fact, it follows that at 1 bar the solidus intersects the two-pyroxene solvus. Schwab (1969) performed experiments on the join $Mg_{1.5}Fe_{0.5}Si_2O_6$–$CaMg_{0.5}Fe_{0.5}Si_2O_6$ and obtained data suggestive of three liquidus fields (O, P, and A), but he did not so interpret the results.

Previous work, natural pyroxenes

Some previous attempts to synthesize the pyroxene phase relations combined data for both pure and impure pyroxene systems. However, based on exploratory experimental runs, Huebner *et al.* (1972) stressed the changes in solidus temperatures and topology caused by variations in minor components, especially Al_2O_3. Thus, quadrilateral phase diagrams based upon data for both pure and natural pyroxene compositions, or upon natural pyroxenes having different minor element chemistries, are likely to be inconsistent unless the effects of the minor components are understood.

Yoder *et al.* (1963) presented what is termed a "working liquidus diagram" based upon data for the synthetic bounding systems, the results of Roedder (1965) for synthetic bulk compositions within the pyroxene quadrilateral, and liquidus determinations using natural pyroxenes. They divided the central pyroxene field into two regions, orthopyroxene (called "protohypersthene") and augite, separated by the boundary curve L(O,A). Pigeonite was not recognized. The orthopyroxene field was carried to the En–Fs join at temperatures in excess of 1400°C, even though Bowen and Schairer (1935), using natural pyroxenes, reported clinopyroxene, rather than orthopyroxene, under these conditions. The following year Yoder *et al.* (1964) published four "preliminary" isothermal sections at 1050°–1350°C. Pigeonite was not identified, but two notable facts are indicated: liquid is present at temperatures as low as 1050°, and at this temperature the entire liquid field projects within the boundaries of the quadrilateral (the liquid field is bounded by fields that include crystalline phases, and does not extend to the Hd–Fs boundary).

Kuno (1966) combined available experimental work, particularly that of Bowen and Schairer (1935) and Yoder *et al.* (1963), with chemical data for coexisting natural pyroxenes. He presented T–X sections which emphasize the pyroxene assemblages in basalts and andesites, and was able to show that the liquidus boundary curves orthopyroxene–pigeonite and orthopyroxene–augite meet to give pigeonite–augite with increasing Fe/(Fe+Mg).

Ross *et al.* (1973) delineated the pigeonite–augite miscibility gap by homogenizing, at successively higher temperatures, exsolved pyroxenes from a lunar basalt. They concluded that the solidus intersects the two-pyroxene (P+A) miscibility gap, thereby confirming Kuno's diagrams. Subsequently, Ross and Huebner (1975, 1979) used natural crystals to investigate the reaction of orthopyroxene with exsolved augite lamellae to form pigeonite. Unlike Bowen and Schairer (1935), they found that melting sometimes accompanied reaction to form pigeonite at 100 Mg/(Fe+Mg) > 65.

Other investigators have contributed valuable insights that help systematize the phase relations of pyroxenes. Nakamura (1971) attempted to explain the observed inversion textures of protoenstatite by proposing the subsolidus reaction on cooling:

protoenstatite + pigeonite → orthopyroxene + augite

Of particular interest is the expansion of the pigeonite field ("Ca-poor Cpx") and movement of an O+P+A field toward the En–Di join with increasing temperature. Although Nakamura's work actually emphasized the subsolidus, we shall see later that the movement of the O+P+A field is an important solidus thermometer.

Albee (personal communication, 1971) constructed a quadrilateral phase diagram (dated June 20, 1969) that shows the liquidus boundary curve originating at the En–Di join and moving toward Hd–Fs as temperature decreases. The boundary curve passes through several quasi-peritectic points (at which the solid phases change), but continues its general trend completely across the quadrilateral to the Hd–Fs boundary. Albee's diagram shows the reaction L + O $\rightleftarrows$ P + A found independently by Huebner and Ross (1972). Most recently, Biggar and Clarke (1971) published a diagram that is similar to that of Kuno (1966), but takes the form of isothermal sections, emphasizing that the Fe/(Mg + Fe) of the liquid increases as crystallization proceeds.

In summary, previous attempts at constructing phase diagrams for the pyroxene quadrilateral succeeded in identifying regions in which orthopyroxene, pigeonite, and augite are stable (Fig. 2). These diagrams failed to account for discrepancies between assemblages predicted from the "pure" bounding systems and the assemblages found in nature. In the following sections, we will attempt accurately to place field boundaries in temperature–composition space, to show the compositions of coexisting phases, and to explain the crystallization paths of liquids that lie outside the quadrilateral plane.

II. Experiments, synthetic pyroxene compositions

Experimental technique

One of us (ACT) has performed melting experiments at 1 bar using synthetic compositions in the system $CaSiO_3$–$MgSiO_3$–$FeSiO_3$ (Table 1).[1] Although the compositions of product phases were not analyzed by microprobe methods, these experiments define most of the divariant reaction surfaces encountered by quadrilateral bulk compositions. We will show that in the pure pyroxene system not only the location of field boundaries, but also the topology of the liquidus surface, differs from that of the natural pyroxene system described later.

Within the impurity limits imposed by the "Analyzed Reagent" grade and subsequent handling, but not crystallization, we consider the starting materials to be pure and to contain the components CaO, MgO, FeO, and SiO_2 in amounts that do not deviate by more than 0.5 relative weight percent from the intended values. All compositions are given in mole percent or atomic fraction, unless otherwise specified. Starting materials were prepared from "Reagent Grade" chemicals. Clinopyroxene and ferrobustamite were crystallized dry at 1 bar using a CO + CO_2 gas mixture to maintain the furnace oxygen fugacity near that of the iron–wüstite assemblage (Turnock *et al.*, 1973). Hedenbergite was crystallized hydrothermally at 1–2 kbar using buffering techniques described by Nolan (1969) and Rutstein and Yund (1969).

As reported previously (Turnock *et al.*, 1973), a single-phase clinopyroxene (or pyroxenoid) could be synthesized for most quadrilateral compositions, demonstrating retention of iron and of cation–oxygen ratio during synthesis. Supporting evidence is the fact that the FeO content of crystallized starting materials ("reactants"), determined by wet-chemical analysis, is within 1 weight percent absolute of the reported composition. Were appreciable iron (as FeO) to have been gained or lost during a run, olivine or silica, respectively, would have been a run product. Single-phase clinopyroxenes did not exsolve on heating for one day at 1100°C. Those single-phase clinopyroxenes having compositions within the pigeonite–augite two-phase region did exsolve, however, in the presence of a small amount of liquid at temperatures 5° to 10° above the solidus; this information permits an estimation of the intersection of the miscibility gap and the solidus.

Where we made individual runs, crystalline starting materials were loaded in iron crucibles or platinum crucibles saturated in iron with respect to the charge composition, or were pelletized and hung on loops of thin platinum wire. The run assemblies were then placed in a hot vertical quench furnace and held at a desired temperature until quenched by gravity drop into water. The temperature measuring circuit was calibrated against the melting points of copper and gold and against the diopside liquidus point, using the IPTS '68 temperature scale. The uncertainty in reported temperatures, including the uncertainty due to the furnace thermal gradient, is less than

---

[1] To receive a copy of Table 1, order document AM-80-131 from the Business Office, Mineralogical Society of America, 2000 Florida Avenue, NW, Washington, D. C. 20009. Please remit $1.00 in advance for the microfiche.

±5°C. The oxygen fugacity within the furnace was maintained at values equivalent to those of the iron–wüstite buffer by passing a $CO + CO_2$ gas mixture through the furnace, using techniques reviewed by Nafziger *et al.* (1971).

Retention of bulk composition was tested under a variety of run conditions. In the subsolidus, loss of iron to the platinum envelope or wire loop, or gain of iron from an iron crucible, could be detected by the appearance of silica or olivine, respectively, where only metasilicates should have been stable. The fact that we retained stoichiometry in the subsolidus confirms previous results reported in Ross *et al.* (1972) and Ross and Huebner (1979, Fig. 4). Independent confirmation of this result is suggested by the wet-chemical analysis of bulk composition $Fe/(Mg + Fe) = 0.50$ and $Wo = 30$, run in pure platinum foil at 1200°C for 1.5 hours. The reactant (glass + augite) and the product augite each contained 22.2 weight percent total iron as FeO (the value calculated for this composition is 21.65 weight percent).

When liquid is present, the problem of iron loss to Pt or iron gain from Fe capsules is potentially more serious, but does not appear to interfere with our results. For 15 runs in iron crucibles, at or above liquidus temperatures, wet-chemical analysis reveals that the charges gained less than 0.4 weight percent iron calculated as FeO, an insignificant amount for most runs. We are confident that under less extreme conditions of temperature, below the liquidus, liquid did not gain significant iron from the iron crucibles. A run in which 0.2 g augite was fused for 0.5 hours at 1364°C in 0.1 g pure platinum foil provides an estimate of the maximum loss of iron to platinum metal: the reactant contained 10.77 weight percent iron as FeO, the product 9.67 percent. This iron loss was minimized in the runs reported in Table 1 by one or a combination of the following procedures: (a) alloy the platinum with iron metal before the run, analogous to the technique of Huebner (1973); (b) "presaturate" the platinum foil by heating it with a large volume of mix of the appropriate bulk composition; (c) reuse foil envelopes; (d) suspend a pellet of reactant on a loop of thin platinum wire, and reuse the wire loop if possible. The most convincing evidence that we were successful in retaining bulk composition is the internal consistency of our results.

Three of the runs reported in Table 1 were made in $Ag_{70}Pd_{30}$ alloy or gold tubes, sealed in evacuated silica capsules. These runs were in the subsolidus and should not have been sensitive to the value of the oxygen fugacity, which was neither controlled nor known. That the run products retained stoichiometry (no silica was observed) argues against oxidation of iron. (We estimate the detection limit of silica by optical microscopy to be 0.1 to 0.5 percent by volume, depending on the location of the silica with respect to other grains.)

Liquidus temperatures were determined by prograde melting experiments. Pellets of crystalline clinopyroxene or pyroxenoid, or the products of previous experiments, were either hung on Pt wire straps or placed in iron crucibles, then loaded into a furnace that had been preheated to the desired run temperature. The pellets suspended by wire straps could be quenched quickly so that crystallization was prevented during cooling. The quenching rate of the charges contained in iron crucibles was not as fast, resulting in the formation of feathery yellow to brown pyroxene during the quench, most pronounced in the iron-rich compositions. After the quench, the run product was examined to determine the proportions of unmelted or recrystallized pyroxene ("phenocrysts") and of melt (now glass and quench pyroxene). Complete melting took place in less than 20 minutes at temperatures >5°C above that of the liquidus for a given composition. The melting was so rapid that prograde experiments alone appear satisfactory. The reaction could be reversed, but undercooling necessary to nucleate crystals was judged to contribute a greater uncertainty in temperature than did the prograde melting reaction.

The solidus was determined as the beginning of melting. Pyroxenes and ferrobustamites form a mosaic (polygonal granular) texture on annealing at subsolidus temperatures. At temperatures above that of the solidus, liquid first forms beads and filaments along the grain boundaries, then coats the pyroxene crystals. Some uncertainty can be caused by the presence of compositional zoning or interstitial impurities (<1% by volume silica) in the starting materials, which causes interstitial liquid to form over a 15°–20°C temperature range. To minimize such uncertainties, the starting materials were annealed, then ground, for four cycles. At worst, these heterogeneities contribute 20°C to the experimental uncertainty. To cause a glassy sample to crystallize completely takes several cycles (grind, heat 4 hours at temperatures below the solidus) to reduce the amount of glass to less than 0.5%.

Reactions at subsolidus temperatures did not proceed quickly; not only are the temperatures the lowest found in this part of the study, but melt is not present to speed material transport. For this reason, the surface between the phase volume of bustamite solid solution and the bustamite–augite miscibility gap was located by prograde reaction.

Pyroxenes were distinguished by conventional optical and X-ray powder diffraction methods. Small amounts of orthopyroxene could be distinguished from clinopyroxene by an extinction position parallel to the trace of prismatic faces or cleavage. The X-ray diffraction pattern of orthopyroxene is so strong and characteristic that it could also be used to identify even small amounts of orthopyroxene in the charge. The presence of polysynthetic twinning is diagnostic of pigeonite, but not all pigeonite grains were twinned, leading to confusion of the two clinopyroxenes during some optical examinations. Augite and pigeonite were, however, reliably distinguished by their X-ray patterns (as in Turnock *et al.*, 1973). Small amounts of augite in the presence of pigeonite were detected by the presence of weak augite (310) and (220) reflections adjacent to the stronger pigeonite (310), ($\bar{3}31$), ($\bar{2}21$), and (220) reflections. The detection of pigeonite in augite could not be done with the same sensitivity. We could best detect pigeonite in amounts greater than ~30% by observing its weak (311), ($\bar{2}31$), and (221) reflections. The intensity of the ($\bar{2}31$) reflection appears to diminish with increasing calcium content of the clinopyroxene; it is weak for Wo = 10, and very weak for Wo = 20. We used the term Cpx in Table 1 to designate clinopyroxene of Wo ≤ 20 percent that showed neither the ($\bar{2}31$) reflection nor polysynthetic twinning. The Cpx could be either $P2_1/c$ pigeonite with an insignificant ($\bar{2}31$) reflection, or an intergrowth of $P2_1/c$ pigeonite and $C2/c$ augite.

Tridymite was identified both by X-ray powder diffraction patterns and by its form (subhedral hexagonal tablets and prisms). Tridymite forms by inversion of cristobalite, which grows first when the mix is crystallized. The inversion takes place only in the presence of liquid, and requires 3 hours at temperatures of 1120° to 1160°C.

Ferrobustamite was distinguished by X-ray powder diffraction methods and by the fact that its refractive indices are lower than those of coexisting augite. That the pyroxenoid is indeed the bustamite with five-unit repeat of Rapoport and Burnham (1973) was confirmed by Malcolm Ross using single-crystal X-ray precession photography.

Phase diagram for synthetic Ca–Mg–Fe pyroxenes

Experimental runs for pyroxene quadrilateral compositions in the synthetic or clean system CaO–MgO–FeO–SiO_2 are presented in Table 1. This table lists bulk composition of run, phases present in the starting materials ("reactant") and in the products of each run, temperature, duration of run, and nature of sample container. The observed run products are plotted in *T–X* sections of the pyroxene quadrilateral (Figs. 3a–h). A liquidus surface (Fig. 4a,c) and a solidus surface (Fig. 4b) were constructed from the *T–X* sections and the results of previous investigators discussed in the introduction and summarized in Figure 2. A complete set of isothermal sections (Fig. 5) was prepared from the preceding figures. In practice, this process was iterative, the earlier sets of diagrams becoming a framework for the planning and interpretation of later runs, until an internally consistent set of *T–X* and isothermal sections could be drawn. The power of this technique was demonstrated by the fact that the existence and position of a number of fields proposed in earlier sets of diagrams were later confirmed by additional experiments. The technique also identified a few initial experiments that contained what appeared to have been a metastable run product. Several runs were repeated, but for longer times, to yield what appear to be stable or at least persistent product assemblages.

We report all observed run products in Table 1 and, on the basis of texture (overgrowth or armoring) or change in proportion during a run, designate some phases as probably metastable. (Those obviously metastable phases that were formed on the quench are not included in Table 1 or indicated by the symbols chosen for Figure 3.) Construction of the *T–X* sections (Figs. 3a–h), however, reveals that textural criteria alone are not sufficient to identify all metastable run products: reasonable and simple *T–X* sections cannot be constructed if Table 1 is assumed to present run products that are all stable assemblages. In a small number of experiments (18), we decided on the basis of phase topology that observed phases are metastable; in 9 of these experiments, the metastable phase is present in small quantities (<3%). Augite is the most common such phase. In 5 experiments, the topology of the *T–X* sections requires that the run products have a phase that was not observed.

Our treatment of these few inconsistent runs will be illustrated by the placement of the boundary between the fields of B and L + B in the section Wo = 50% (Fig. 3e). In two runs [Fe/(Mg + Fe) = 80%, 1160°C; Fe/(Mg + Fe) = 90%, 1152°C] we detected small amounts of liquid, yet the temperatures are too low to be consistent with the L + B field on the liquidus (Fig. 4a) or the section Wo = 40% (Fig. 3f). We

Figure 3a-h. Temperature-composition sections with results of experiments on pyroxene quadrilateral compositions in the pure system CaO-MgO-FeO-SiO_2 at one bar pressure and low oxygen fugacity. The ratios 100Fe/(Mg+Fe) and Wo = 100 Ca/(Ca+Mg+Fe) are in atom percent. Symbols refer to run product phase "assemblages" thought to be stable on textural evidence; the symbol key is used consistently throughout all figures. Simple symbols refer to one phase assemblages and and occur either in the subsolidus or above the liquidus. Assemblages that contain melt are identified by a circle. The presence of silica (tridymite) is indicated with a darkened center - such as the dot in the symbol for BS and LBS, or the polyphase assemblages are combinations of symbols for the constituent phases. Clinopyroxene (Cpx) is used when augite and pigeonite could not be distinguished, and could also designate a mixture of augite and pigeonite. The temperature is in °C.

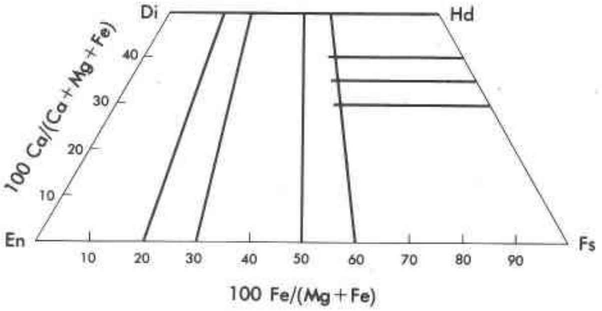

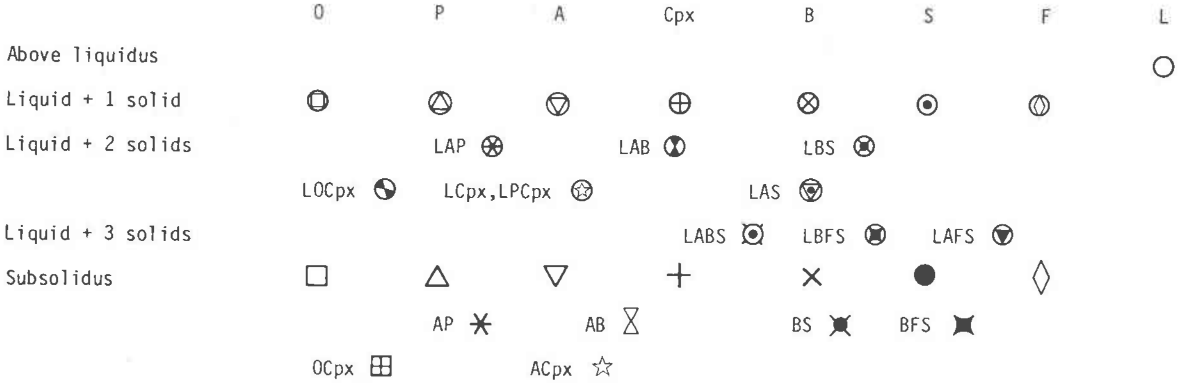

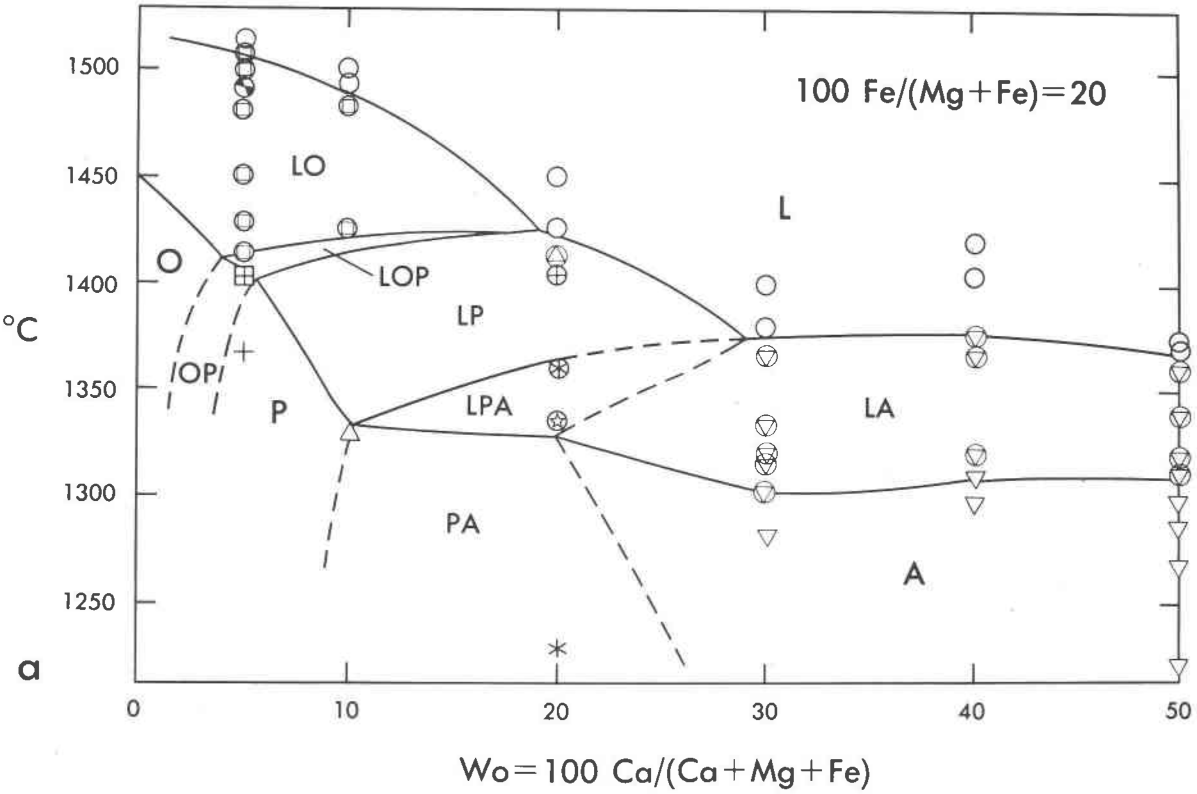

Fig. 3. (continued)

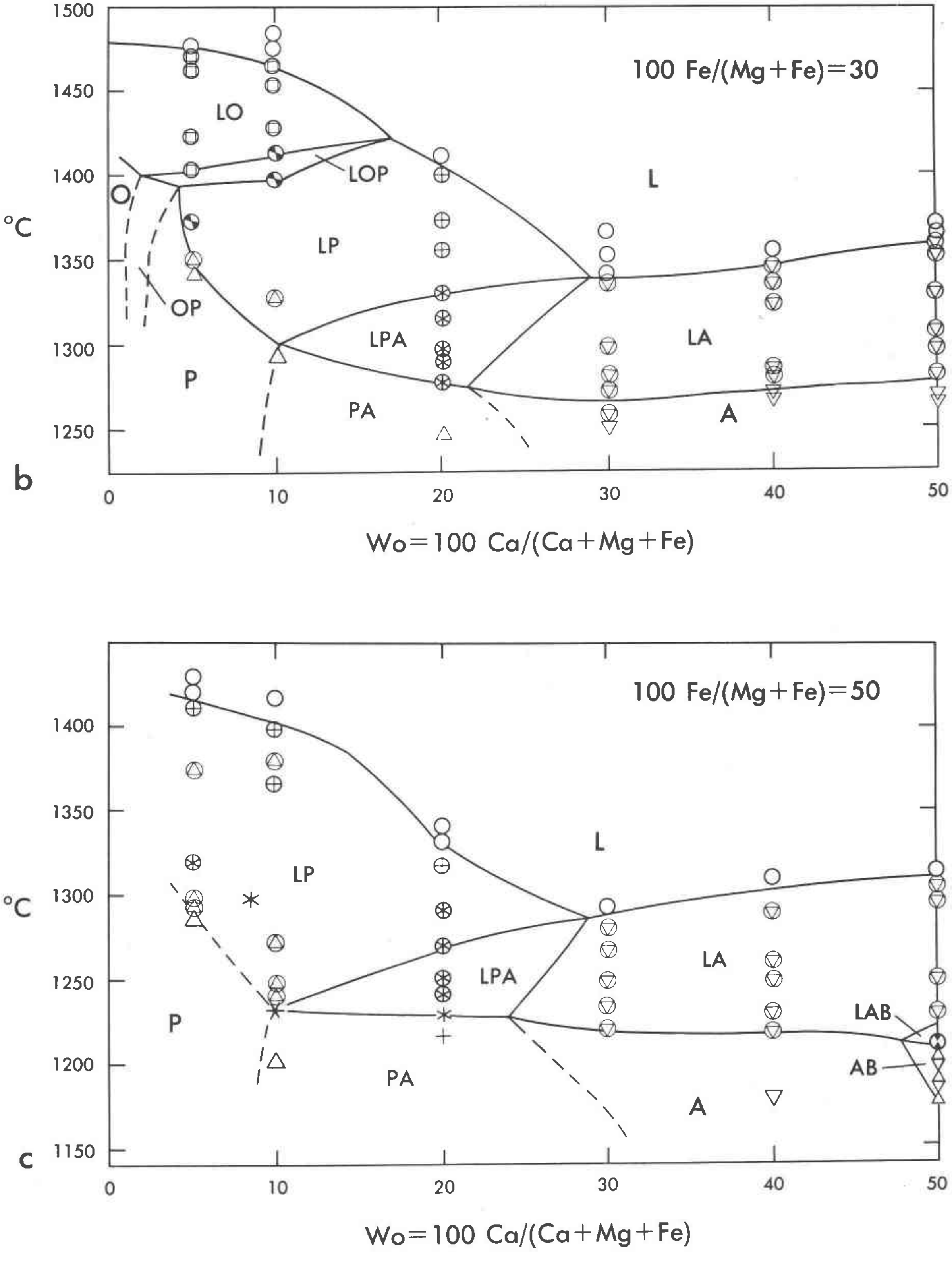

Fig. 3. (continued)

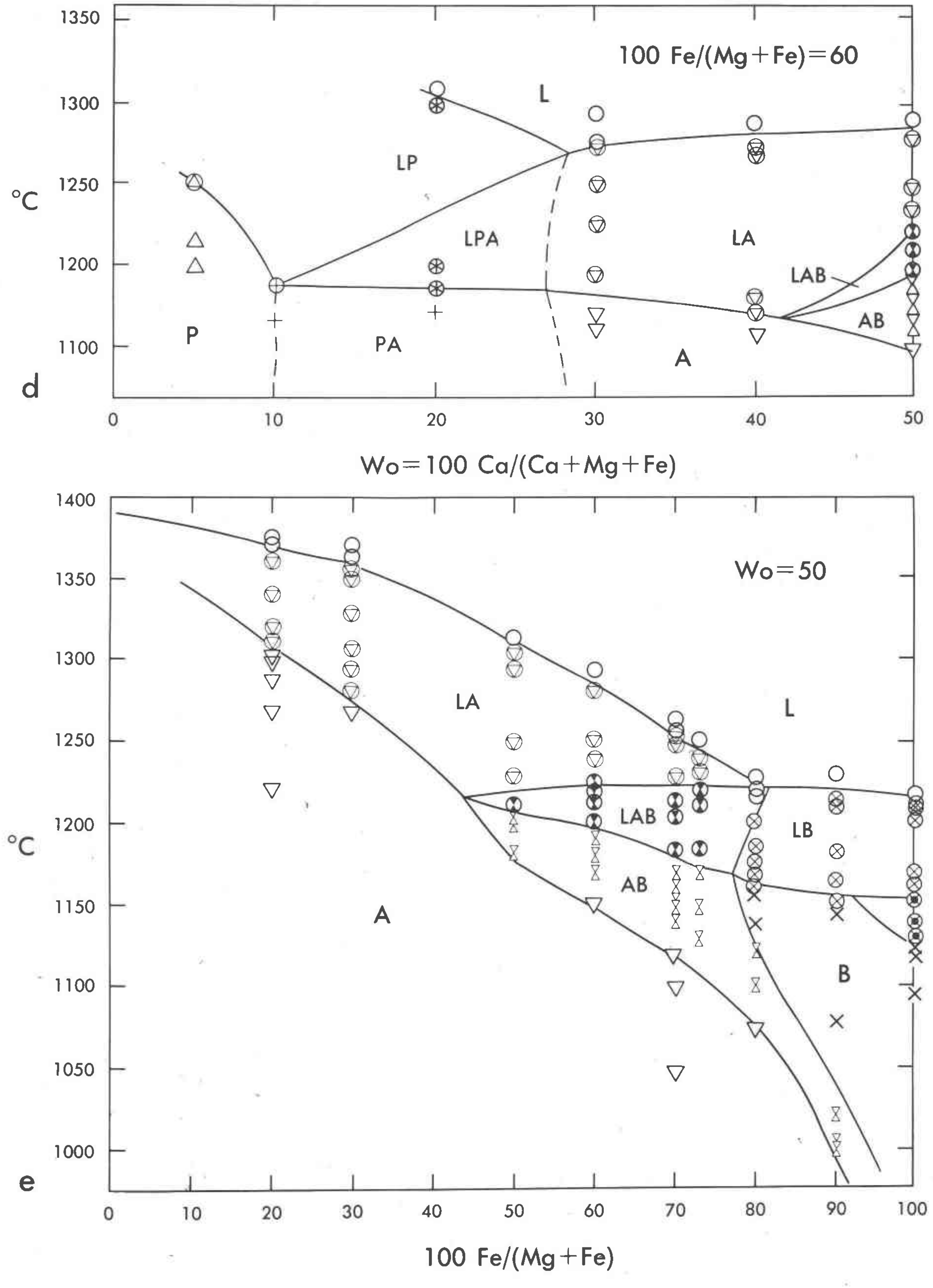

Fig. 3. (continued)

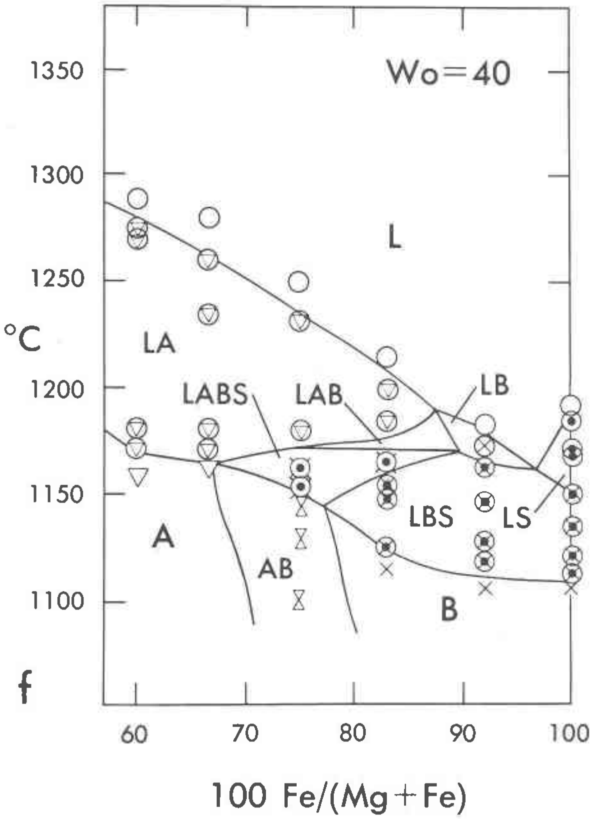

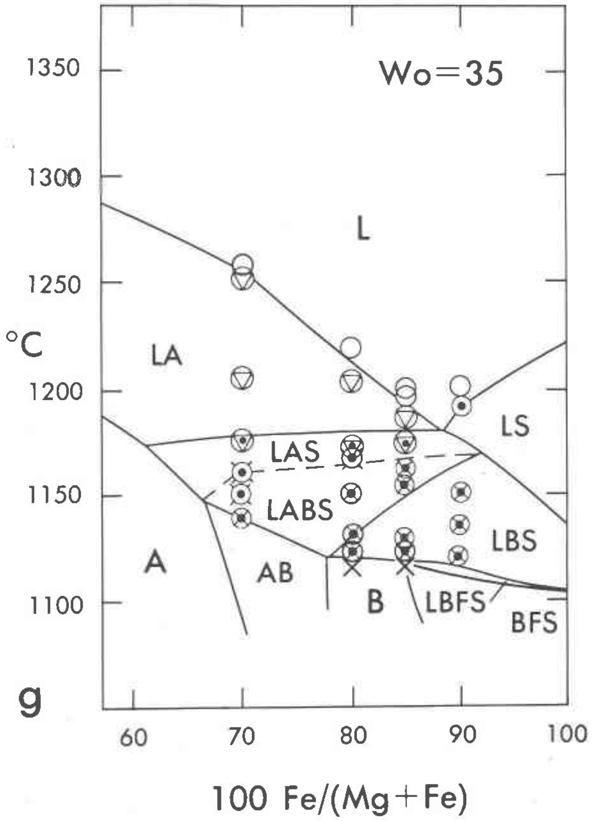

attribute the melt observed in the run at 1152°C to be due to heterogeneous starting material, as previously described. We attribute the melt in the run at 1160°C to the observed, texturally metastable augite; the augite is relatively magnesian, causing the composition of the bustamite to become enriched in iron and thus melt at a temperature that is beneath the solidus temperature for the bulk composition of the runs.

Liquidus

The liquidus surface of the pure pyroxene system is divided into six primary-crystal fields, F, O, P, A, B, and S (Fig. 4a). Isotherms were based on runs reported in Table 1 and the previously determined bounding systems (Fig. 2a) and appear to be internally consistent. Where experimental control is available, appropriate isotherms pass within 1 mole percent (or 10°C) of each datum. The liquidus fields drawn in Figure 4a agree completely with the primary crystalline phases observed experimentally. In general terms, we describe the liquidus in Figure 4a as decreasing in temperature from En to the magne-

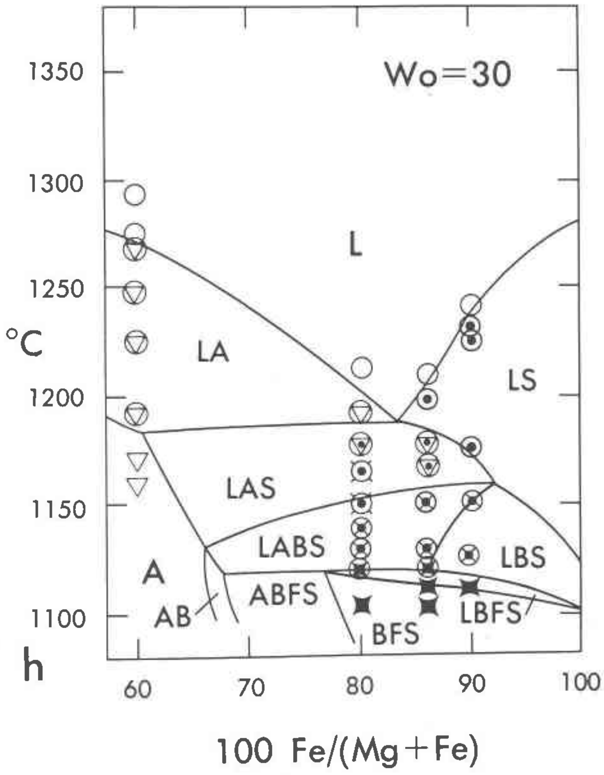

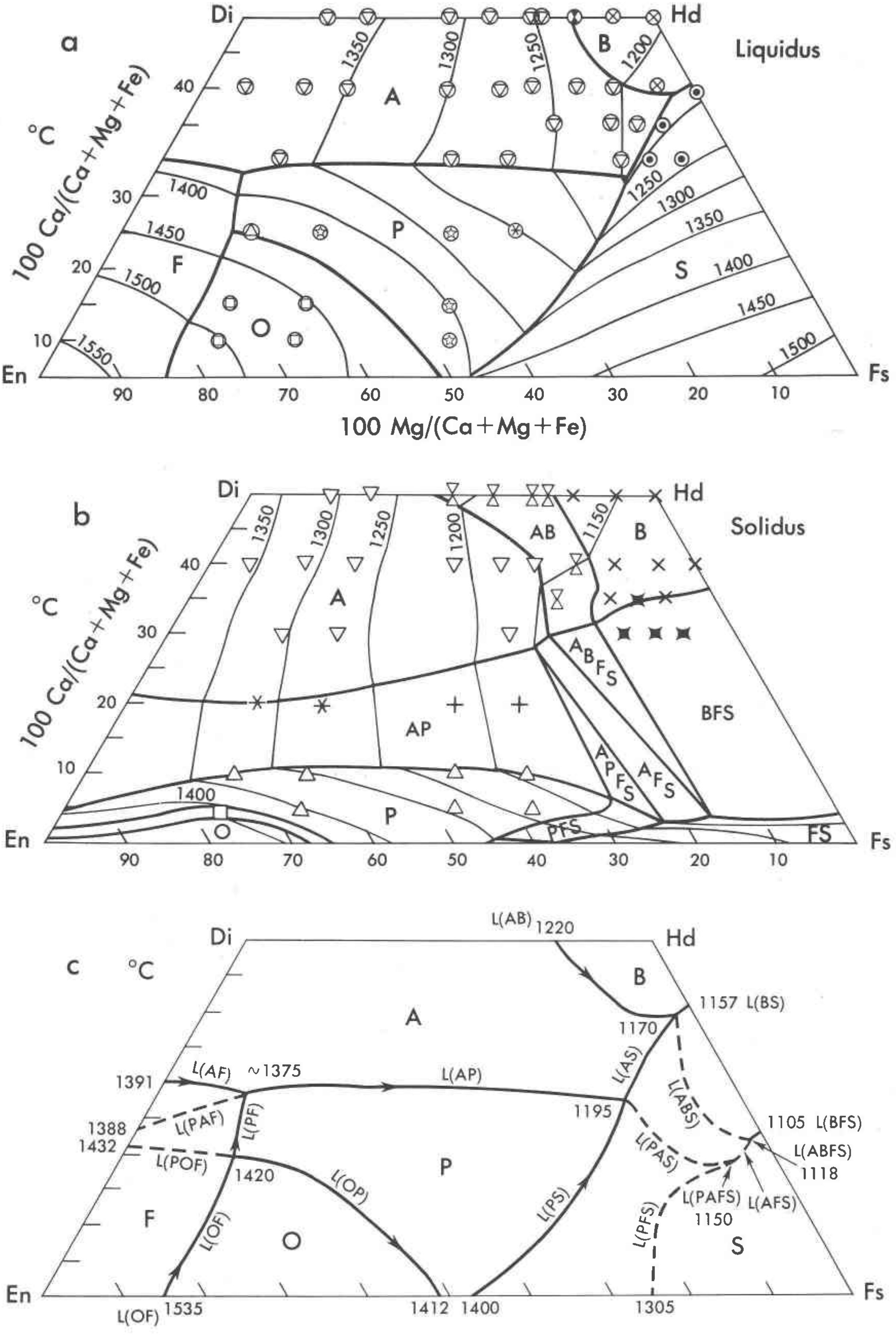
a
Liquidus
Di
Hd
En
Fs
°C
100 Ca/(Ca+Mg+Fe)
100 Mg/(Ca+Mg+Fe)
A
B
P
F
O
S
1200
1250
1300
1350
1400
1450
1500
1550
b
Solidus
AB
ABFS
BFS
AP
APFS
AFS
PFS
FS
1150
1200
1250
1300
1350
1400
c
L(AB) 1220
1157 L(BS)
1170
L(AS)
L(ABS)
1391
L(AF)
~1375
L(AP)
1195
1105 L(BFS)
L(ABFS)
1118
1388
L(PAF)
L(PF)
L(PAS)
1432
L(POF)
1420
L(OP)
L(PS)
L(PAFS)
L(AFS)
1150
L(PFS)
L(OF)
L(OF) 1535
1412
1400
1305
10
20
30
40
50
60
70
80
90

sium-free join near Hd. (Liquidus temperatures near Fs are also high, but such ferruginous bulk compositions are not relevant geologically.) The olivine field is bounded by L(A,F), L(P,F), and L(O,F) which intersect to form the reactions $F + L \rightleftarrows O + P$ (pseudo-quasi-peritectic) and $F + L \rightleftarrows A + P$ (pseudo-peritectic); the terminology is that of Prince (1966). At magnesium-poor compositions, the points L(A,P,S) and L(A,B,S) are encountered. L(B,S) continues to the minimum liquidus temperature, 1154°C, which is at the magnesium-free join Hd–Fs.

The extent of the olivine field (labelled "F" in Fig. 4a) is much smaller than that shown by Roedder (1965). We did not find olivine on the liquidus in experiments with compositions along the join Fe/(Mg + Fe) = 0.20 (Fig. 3a); olivine is thus restricted to bulk compositions with Fe/(Mg + Fe) < 0.20. Roedder found liquidus olivine at bulk composition $Wo_{26}En_{41}Fs_{33}$. That particular bulk composition was slightly deficient in silica (p. 699) before the liquidus determination. His final reaction heating experiments were performed with a small amount of glass mix contained in iron foil envelopes. If the charge gained iron (as FeO) from the container during the run, the bulk composition would have moved even farther from the pyroxene quadrilateral plane toward the olivine plane (Fig. 1), and most probably into an olivine liquidus field (see Bowen and Schairer, 1935, p. 159). We tested the effect of excess FeO by adding an amount of FeO equivalent to 3 percent by weight of sample to the composition $Wo_{10}En_{72}Fs_{18}$. This doped run produced 40% olivine + 60% glass at 1500°C, whereas for compositions without excess ferrous iron, the liquidus is at a slightly lower temperature (1490°), and orthopyroxene is the primary phase. We conclude that the anomalously large olivine field found by Roedder could be due to the charge gaining a small amount of iron as FeO from the iron foil containers.

We found that orthopyroxene is the primary crystal phase on the liquidus at calcium-poor bulk compositions [Wo = 5–20 and Fe/(Fe + Mg) = 0.20 and 0.30]. Williams (1971, p. 355) implied that orthopyroxene is the solidus pyroxene in his experiments on the system $Fe–MgO–SiO_2–O_2$. Bowen and Schairer (1935) showed clinopyroxene to be the liquidus phase at Wo = 0; they probably crystallized protopyroxene, which inverted to clinopyroxene on quenching. Moving into the quadrilateral from the En–Fs join, the orthopyroxene (O) field never meets the augite (A) field, being separated from it by the pigeonite (P) field. A consequence of this fact is that O + A cannot coexist in equilibrium with a liquid of metasilicate composition, despite the fact that O + A is a common equilibrium association during the early crystallization of tholeiitic lavas and intrusions (Wager and Deer, 1939; Nakamura and Kushiro, 1970).

We place the lowest liquidus temperature on the Hd–Fs join, rather than within the quadrilateral, because lower liquidus temperatures have been observed on the Hd–Fs join than within the quadrilateral. The lowest liquidus temperature found by Bowen *et al.* (1933) for compositions approximating the metasilicate join $CaSiO_3–FeSiO_3$ was 1167°±4°C (their Table 1, p. 199) at Fe/(Ca + Fe) = 0.571. In their *T-X* section (their Fig. 8), the curves L(B) and L(S) intersect at approximately 1160°C (p. 215). Bowen *et al.* chemically analyzed the glasses that they produced just above the liquidus and found them to be close to $(Ca,Fe)SiO_3$ composition; we do not believe that the compositions of their runs at lower temperatures differ significantly from the reported liquidus compositions [the temperature of the curve L(B,S) is sensitive to composition in the ternary system $CaO–FeO–SiO_2$]. We found 1154°±7°C as the temperature at which L(B,S) reaches the magnesium-free join, in essential agreement with the value of 1160°±5°C found by Bowen *et al.* Within the quadrilateral, we observed no liquidus temperatures lower than 1178°±5°C. Thus, we draw L(A, B,S) as a pseudoperitectic at 1170°C and show L(B,S) passing outward to the join Hd–Fs at 1157°C.

Our experiments do not control the positions of L(O,P) and L(P,S) near the En–Fs join. These two curves can either reach the calcium-free join or intersect within the quadrilateral to generate L(O,S). We have elected the former alternative because it slightly simplifies our diagrams and because Bowen and

Fig. 4. Liquidus and solidus surfaces for pyroxene quadrilateral (metasilicate) bulk compositions in the pure system $CaO–MgO–FeO–SiO_2$ at one atm and low oxygen fugacity. Projections of bulk compositions used for the present investigation are indicated by the positions of the run symbols. The positions of isotherms and the nature of the liquidus and solidus phases are based on runs of Table 1 (Fig. 3) and previous investigations (text and Fig. 2). Fig. 4a, liquidus diagram; Fig. 4b, solidus diagram; Fig. 4c, projection showing paths of liquids that coexist with two solid phases (solid curves) or three solids (dashed curves). The solid curves lie in the pyroxene quadrilateral plane; the dashed lines lie above or below the pyroxene, depending upon whether the liquid is depleted or enriched in silica relative to the metasilicate bulk composition. The temperature is in °C.

Schairer (1935, p. 155) report the coexistence of tridymite, clinopyroxene, and liquid at 1400°C and 60 weight percent $FeSiO_3$ in the calcium-free system. Although we later note that Bowen and Schairer may not always have correctly identified the nature of pyroxene present *before* quenching, we have no reason to suspect a discrepancy here.

Solidus

The solidus surface (Fig. 4b), like the liquidus, is derived from Figures 3a–h. As in the liquidus diagram, the positions of solidus fields and isotherms were controlled by experiments shown in Table 1 (and Fig. 3) and data for the bounding systems discussed previously (text and Fig. 2). In only one experiment is there a conflict between the experimentally observed run products (Fig. 3g) and the fields shown on the solidus (Fig. 4b). At Wo = 35, Fe/(Mg + Fe) = 0.80, and 1123°C, the phases bustamite and silica, but not olivine, were observed; the correct solidus assemblage is apparently bustamite + olivine + silica.

The ternary one-phase fields O, P, A, and B, and the quaternary two-phase field F + S, are separated by prominent miscibility gaps. We found no evidence that the P + A miscibility gap or "solvus" closes completely with increasing Fe/(Mg + Fe) to leave a region of clinopyroxene solid solution on the solidus, a suggestion made by Grover *et al.* (1972) for conditions at 15 kbar. The *T–X* section at Fe/(Mg + Fe) = 0.60 (Fig. 3d) includes experiments in which clinopyroxene solid solution reacted to form two pyroxenes and melt. The sections at Wo = 30 percent and 35 percent (Figs. 3g,h) show that the augite field passes into fields bearing olivine and silica; no pigeonite-bearing fields were detected. If there is complete closure of the miscibility gap, it must occur over a narrow range of Fe/(Mg + Fe) values greater than 0.60.

Experimental control on the tieline configuration between P, A, or B, and F + S at the solidus is not good in the pure system. We have shown augite to coexist with olivine + silica (rather than pigeonite with bustamite) because the assemblage A + F + S occurs in metamorphosed iron formation (Bonnichsen, 1969), in the products of partially melted natural pyroxenes (Part III, this work), and in the assemblage A + B + F + S at 1130°C, just beneath the solidus in the pure pyroxene system (D. H. Lindsley, personal communication, 1974.).

The only previously reported experiments pertaining to the solidus within the quadrilateral are those of Schwab (1969, p. 249) on the join $Mg_{1.50}Fe_{0.50}Si_2O_6$–$CaMg_{0.5}Fe_{0.5}Si_2O_6$. He distinguished pyroxenes by X-ray diffraction and showed that, as in the present investigation, with increasing $CaSiO_3$ the solidus fields of orthopyroxene, pigeonite, augite, and augite + bustamite are successively found. Schwab's solidus temperatures agree with our results only for calcium-poor compositions. We do confirm the existence of "wollastonite" (or a pyroxenoid) at composition $Ca_{1.0}Mg_{0.5}Fe_{0.5}Si_2O_6$ on the solidus, but we observed the solidus at 1208°±3°C, whereas Schwab found it at 1275°±25°C. The results of Bowen and Schairer (1935) for the En–Fs join disagree with our results by showing a clinopyroxene solidus at Wo = 0, Fe/(Mg + Fe) = 0.04–0.53. We suggest that at least in the range Fe/(Mg + Fe) = 0.2–0.3, Wo ≤ 2%, an orthorhombic pyroxene is the stable solidus phase, and that Bowen and Schairer may have observed inverted protopyroxene. Protopyroxene forms in calcium-free pyroxene systems at temperatures greater than ~1150°C and transforms to pigeonite on quenching.

Quaternary equilibria

None of the endmembers, or their solid solutions, melts to a liquid of identical composition: nowhere do the liquidus and solidus surfaces meet in the quadrilateral. The pyroxene phase relations can be understood only in terms of the quaternary system CaO–MgO–FeO–SiO_2. In an effort to indicate the quaternary phase relations that occur between the liquidus and solidus (Fig. 4a, b, respectively), we show all loci of compositions of liquids that are in univariant equilibrium with two (ternary) and three (quaternary) solid phases by projection from silica in Figure 4c. The solid lines are the same phase boundaries that are shown on the quadrilateral liquidus (Fig. 4a) and refer to liquids that lie on the pyroxene composition plane. Because the system bulk composition is constrained to the pyroxene quadrilateral plane, liquids that actually coexist with olivine or silica (as distinguished from liquids that could coexist) cannot have compositions that plot on the pyroxene plane and therefore must be quaternary. The dashed boundaries represent projections of quaternary liquids that coexist with three solids. In quaternary *T–X* space, these curves lie within the volume bounded by the liquidus and solidus surfaces. Such dashed boundary curves are actually segments of four-phase quaternary isobaric univariant liquidus curves that pass through the piercing points L(O,P,F), L(P,A,F), L(P,A,S), and L(A,B,S) on the pyroxene quadrilateral liquidus. These segments of curves appear to originate from, rather than pass through, the piercing points because the system requirement of pyroxene bulk composition restricts the composition of the liquid to only one side of the pyroxene plane. The presence of an undersaturated solid requires the liquid to be enriched in silica, and *vice versa*. From these diagrams (Figs. 4c and 5) we can deduce the direction in which the quaternary univariant liquids move as their composition passes through the pyroxene plane with decreasing temperature.

The field boundaries in the liquidus diagram (Fig. 4a) for the pyroxene plane are surfaces in the quaternary system. Each of the univariant curves piercing the quadrilateral plane is defined by the intersection of three such surfaces. Thus, L(A,B,S) has in common the planes L(A,B), L(A,S), and L(B,S).

The quaternary equilibrium liquidus point L(A,B,F,S) is shown (in Fig. 4c) projected into the interior of the quadrilateral; it would be most improbable to find this five-phase assemblage in the bounding system CaO–FeO–SiO_2 at 1 bar pressure, and such a relationship has not been observed in experiments on this system. The quaternary liquidus curve L(B,F,S) leaves L(A,B,F,S) and, with decreasing temperature, approaches the CaO–FeO–SiO_2 plane, meeting it at the experimentally determined temperature of 1105°C (Bowen *et al.*, 1933), the lowest temperature at which liquid has been detected in a system of pure pyroxene bulk composition. The solidus surface of ferrobustamite slopes down-temperature from Mg-bearing compositions towards the Mg-free compositions (see Fig. 3f), which indicates that the lowest solidus temperature is Mg-free. This topology is consistent with the experimental observation (this paper) that in impure (or natural) pyroxene systems, the liquid in the assemblage L(B,F,S) projects onto the quadrilateral plane at less magnesian compositions than either the olivine or the metasilicate, even when the liquid composition has <4 percent (mole) $MgSiO_3$.

The departure of the liquid composition from the pyroxene plane can be illustrated by considering the positions of liquid paths near $MgSiO_3$ bulk composition. $MgSiO_3$-rich compositions melt incongruently to olivine plus a liquid that is enriched in silica relative to the pyroxene plane. The greater the proportion of forsterite present, the greater is the departure of the liquid from the pyroxene plane toward silica. The olivine field is bounded, however, by the L + O, L + P, and L + A fields, in which olivine is not present. The three pyroxenes have metasilicate composition, thus the coexisting liquids must also lie in the metasilicate plane so that metasilicate bulk composition is conserved. As the temperature decreases, the liquidus paths L(O,P,F) and L(P,A,F) move from the iron-free sideline toward the pyroxene field (Fig. 4c). In this temperature interval, the liquid composition gradually approaches that of metasilicate by reacting with olivine. At the piercing points L(P,A,F) and L(O,P,F), the liquid has metasilicate composition. Because the pyroxene system is restricted to metasilicate bulk compositions and no silica-rich phase is present at the piercing points, the liquid path cannot pass through the pyroxene plane to silica-deficient compositions.

Isothermal sections

We have chosen isothermal sections to illustrate the phase relations of metasilicate bulk compositions in the pure system CaO–MgO–FeO–SiO_2 (Fig. 5). The plane of the sections is the pyroxene quadrilateral plane, which contains the bulk compositions. Several elements shown in the diagrams can be considered to be coincident with the plane of section. These elements are the one-phase fields of orthopyroxene, pigeonite, augite, ferrobustamite, and liquid, which have compositions that do not depart significantly from metasilicate composition. The one-phase field, liquid, exists on the plane because its composition is restricted to be that of a metasilicate. Removal of this arbitrary constraint expands the liquid plane to a volume that lies above and below the metasilicate plane.

Two-phase volumes such as L + F and L + S, which involve compositions that plot off the metasilicate plane, are each defined by a set of tie-lines that are not necessarily parallel, but that pass through the pyroxene plane. The surfaces of these volumes may be irregular, appearing as curved field boundaries in the isothermal sections. Three-phase volumes such as LPF and LAS are bounded by sets of tie-triangles that do not lie in the pyroxene plane. The bounding surfaces are composed of the sides of tie-triangles. In isothermal section, the field boundaries are curved except where adjacent to a four-phase volume or where one side of the triangle lies in the plane of the section. In these exceptions, the boundaries are straight lines. Four-phase volumes such as LAFP and LAPS are each bounded by four tie-triangles to form irregular, six-edged volumes. Isothermal sections through these four-phase volumes must appear triangular; quadrilateral sections through these volumes cannot occur because the pyroxene system contains no four-phase assemblages that have all

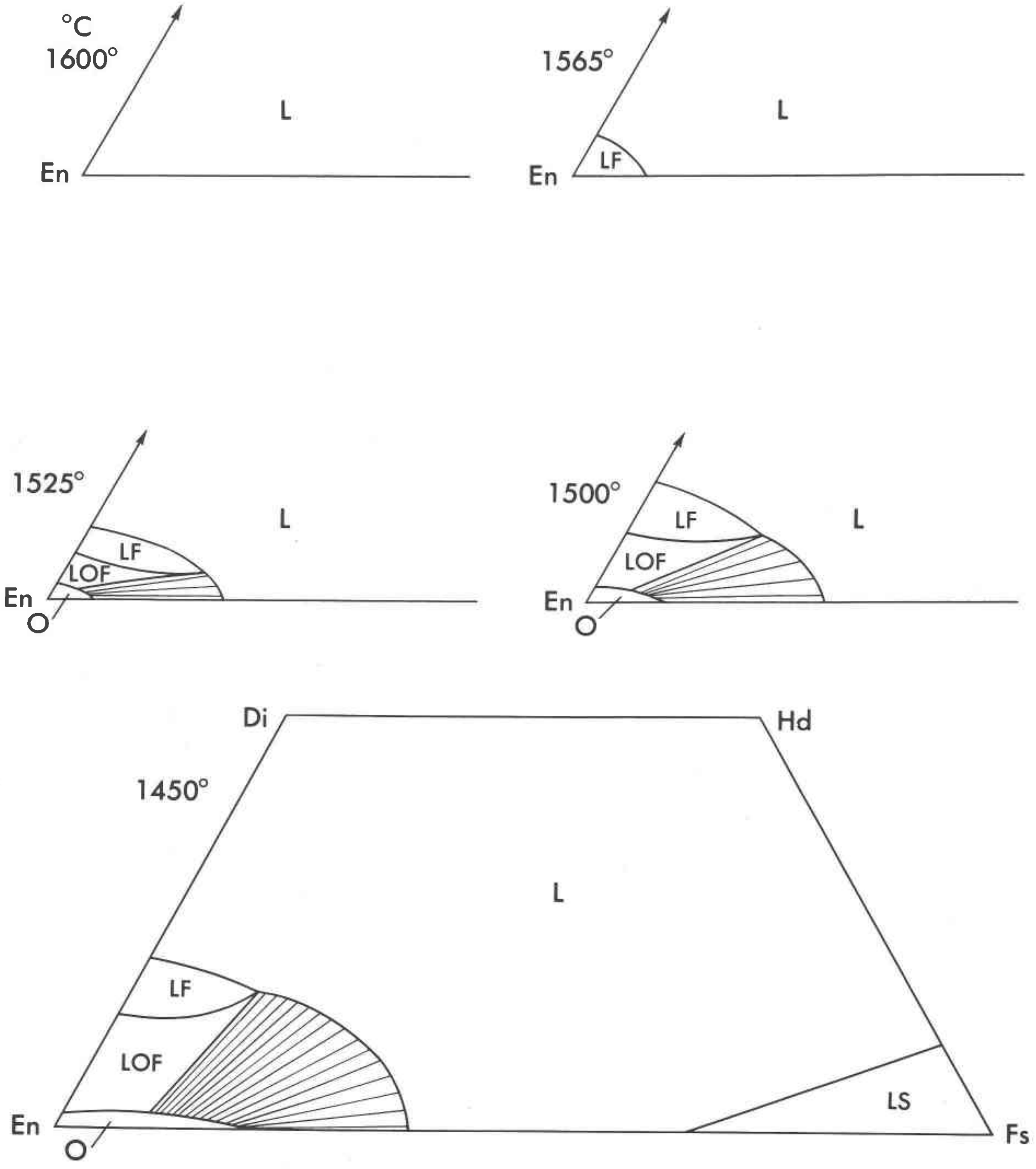

Fig. 5. Isothermal sections for the pyroxene quadrilateral (metasilicate) plane in the system CaO–MgO–FeO–SiO_2. The sections reflect the topology presented in Fig. 4c and are based upon new data presented in this paper (Fig. 3; Table 1) and previous results (Fig. 2; discussed in text). Two-phase assemblages that lie in the pyroxene plane are ruled; tie-line orientation within the two-phase region is schematic. Temperatures are in °C.

Fig. 5. (continued)

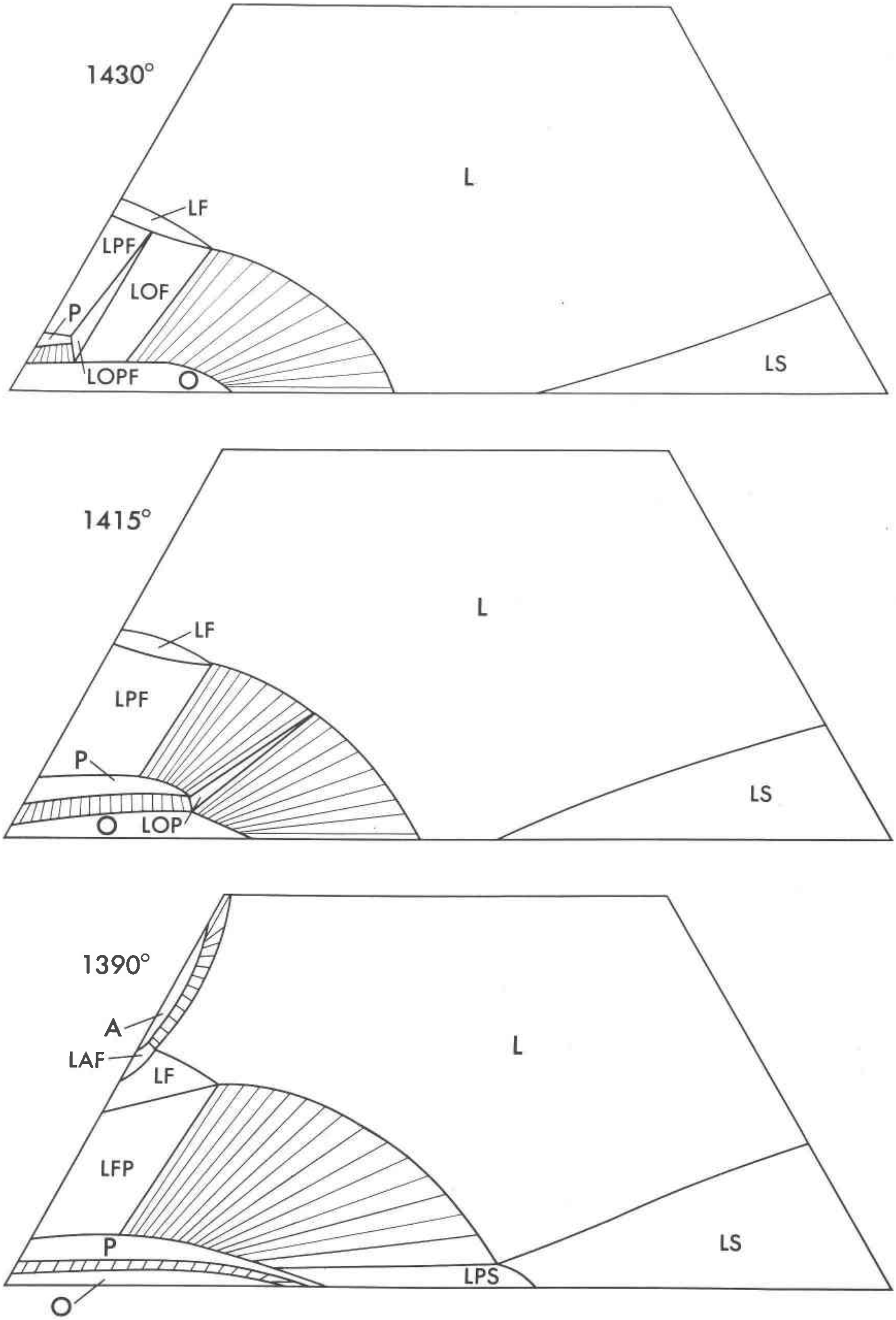

Fig. 5. (continued)

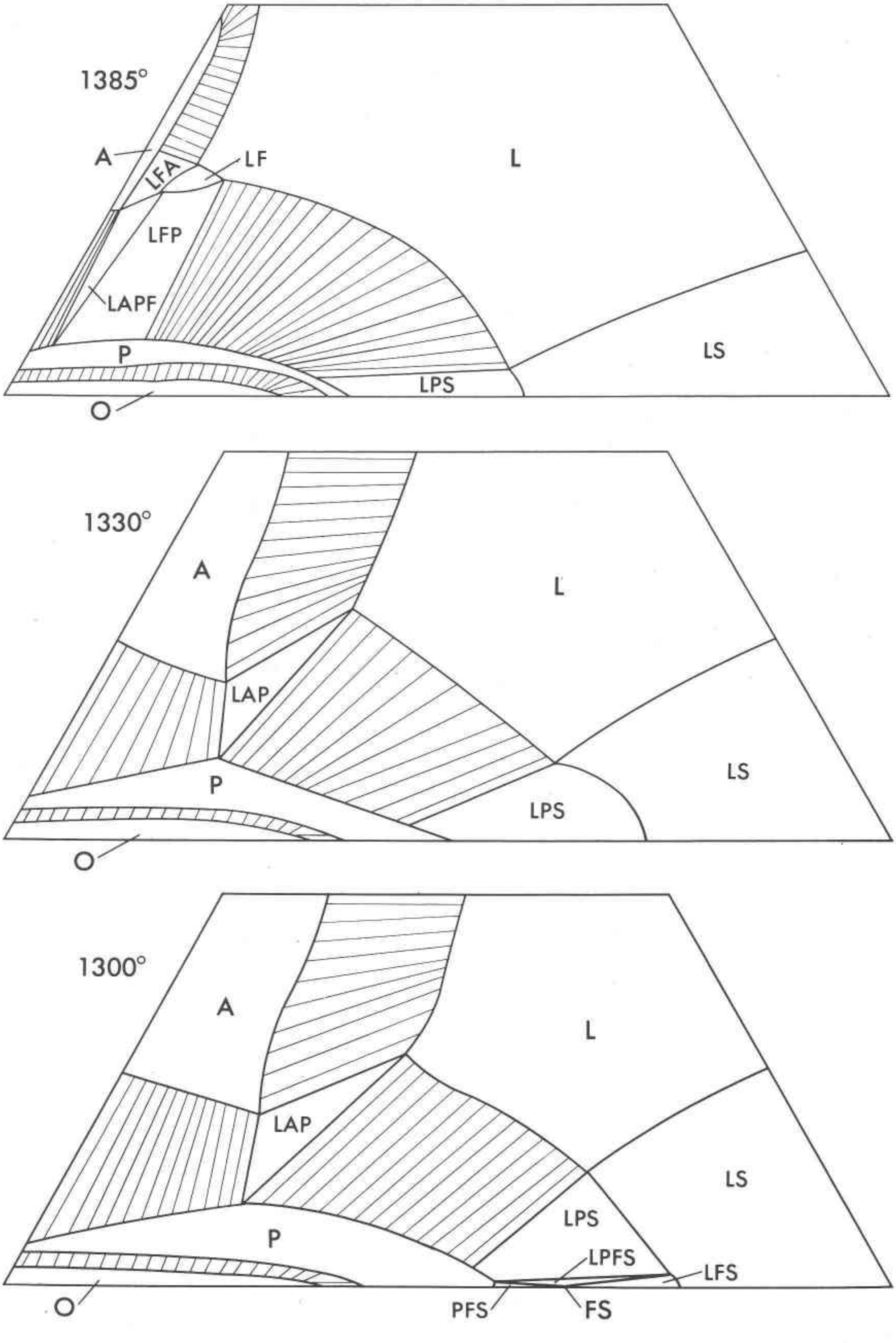

Fig. 5. (continued)

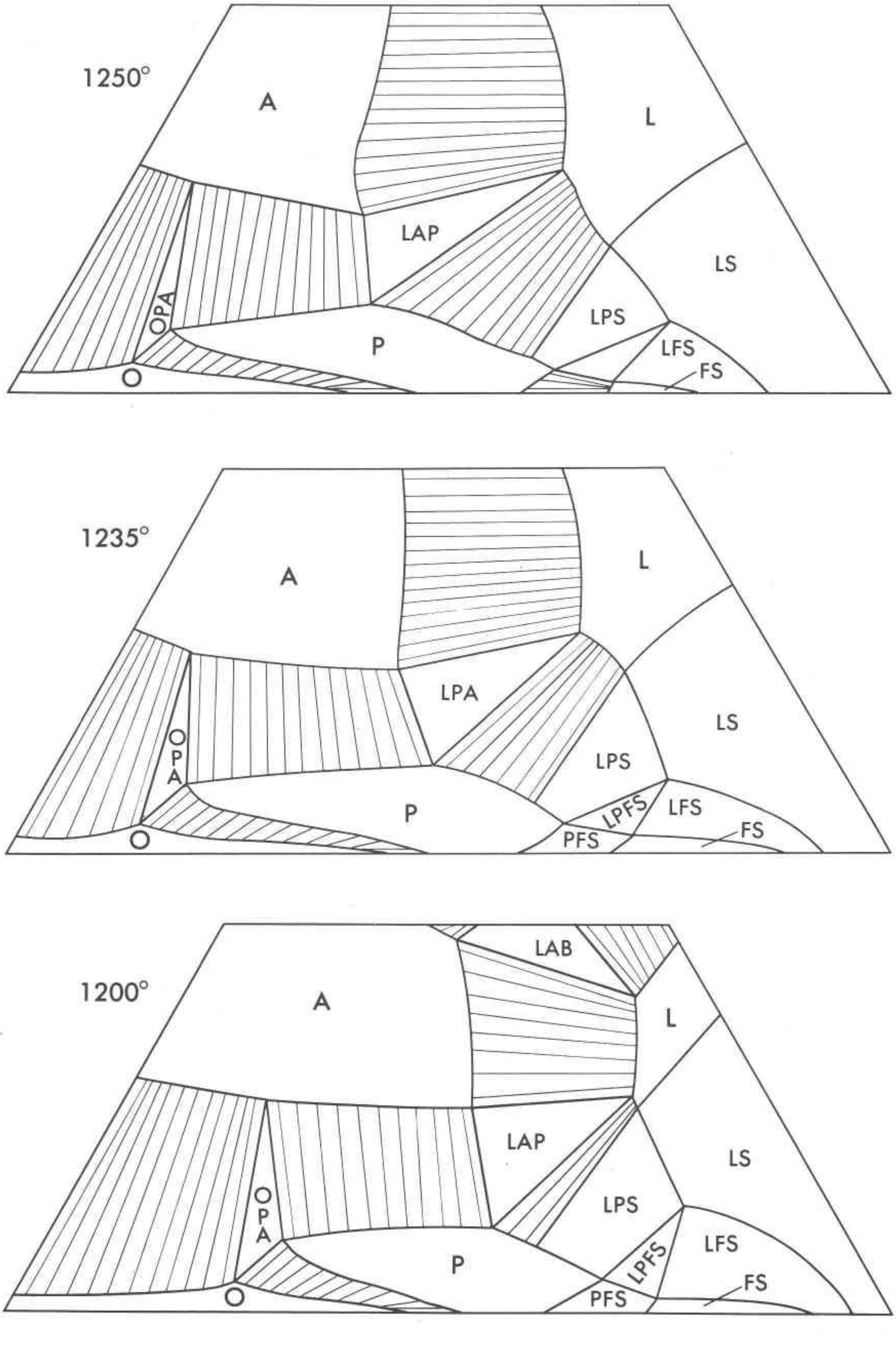

Fig. 5. (continued)

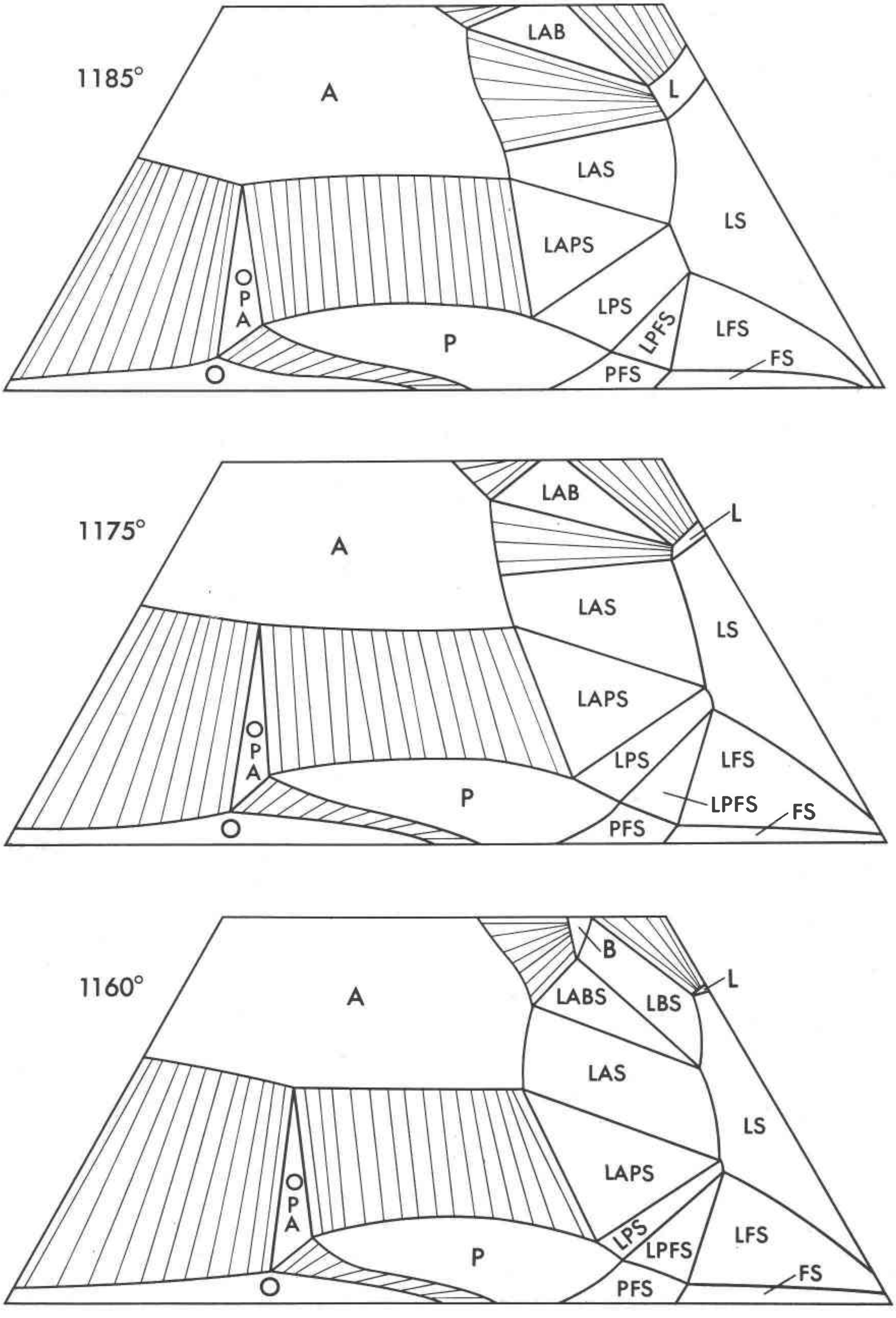

Fig. 5. (continued)

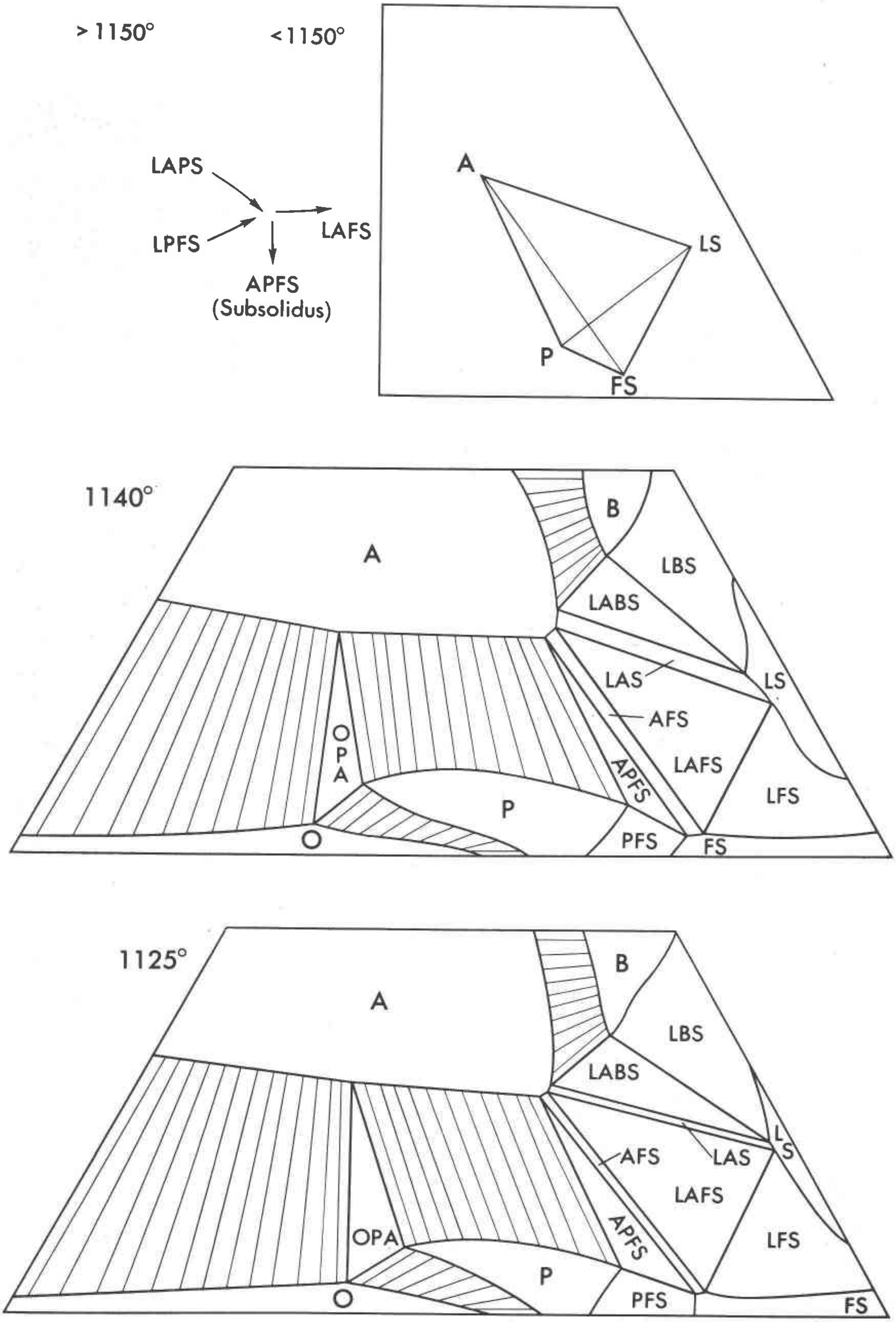

Fig. 5. (continued)

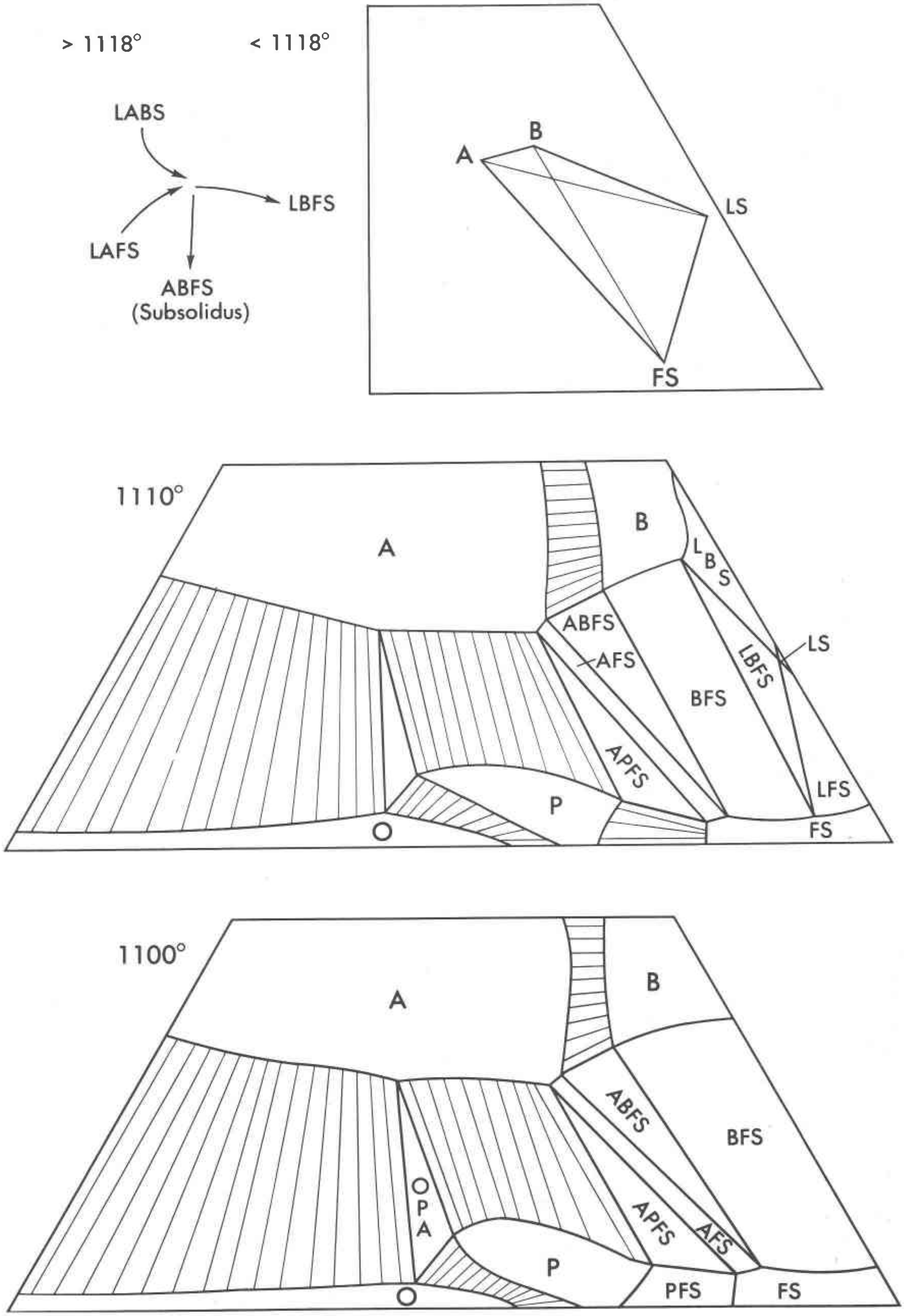

compositions plotting off the pyroxene plane (two plotting above and two below).

The shapes of the various volumes that lie between the liquidus and solidus surfaces can be seen by examining the isothermal sections for compositions near the $MgSiO_3$-rich part of the diagram (Fig. 5). At 1600°C all points in the system are above the liquidus. Forsterite crystallizes from $MgSiO_3$ composition at 1577°C; as the temperature is lowered progressively, more iron- and calcium-rich compositions begin to precipitate olivine. The section at 1525° intersects the L(O,F) cotectic. Liquids in equilibrium only with orthopyroxene lie in the pyroxene plane. The volume L + O + F is defined by a set of tie-triangles. The most iron-rich tie-triangle has its side L + O in the plane of the section; this liquid lies in the pyroxene plane, although it is in equilibrium with (an infinitesimal quantity of) olivine. More magnesian bulk compositions of L + O + F involve greater amounts of olivine and a liquid that is more siliceous than the metasilicate pyroxene plane. The boundary between the L + F and L + O + F fields is formed by the set of L + F tie lines that is in equilibrium with orthopyroxene. It is not a projection from silica of the liquid composition (it would be fortuitous if the olivine and liquid compositions were collinear with silica). We do not know the orientation of the L + F tie lines, so this boundary is only schematic.

Pigeonite begins to crystallize at 1532°C (Yang and Foster, 1972, p. 1239). As the temperature decreases, the volume L + F + O + P moves into the quadrilateral. Pigeonite and orthopyroxene lie in the pyroxene plane; olivine and liquid plot below and above the plane, respectively. Thus, LFOP appears triangular in the isothermal section. Again, the liquid composition cannot be determined from the diagram because the orientation of the edge L + F is unknown. (In Fig. 4c, the dashed quaternary liquidus curves are estimated projections from silica and indicate, in a topological sense, the Ca:Fe:Mg of the liquid.) As the temperature continues to decrease, olivine and orthopyroxene react with liquid to precipitate pigeonite; all olivine is exhausted as L(O,P,F) reaches the piercing point on the pyroxene plane and the liquid acquires metasilicate composition. Further crystallization follows L(O,P), within the pyroxene plane. Orthopyroxene reacts out, and pigeonite precipitates until all liquid is consumed.

Subsolidus

We know of very little low-pressure experimental data for the subsolidus of the pure system CaO–FeO–MgO–SiO_2; such studies are hindered by metastability and extremely slow rates of reaction. Simmons *et al.* (1974) "reversed" the reaction: synthetic pigeonite $\rightleftarrows$ orthopyroxene + augite at 800°C and Fe/(Mg + Fe) = 0.75 (bulk composition). Because the formation of pigeonite was accompanied by olivine + quartz, their bracketing "reversal" occurred with respect to changing Fe/(Mg + Fe). We do not know the limits of Fe/(Mg + Fe) in their experiments, but do not expect them to be large. Grover (1972) investigated synthetic low-temperature "clinoenstatite," finding it to be stable relative to orthopyroxene in $MgCl_2 \cdot H_2O$ flux below 556°C. Because he restricted his bulk compositions to iron-free compositions, and because pigeonite is not known to be stable geologically under these conditions, we did not attempt to incorporate this work in our diagrams for the interior of the quadrilateral. We note, however, that this low clinoenstatite could be a continuation of the high-temperature pigeonite field.

More comprehensive data for the subsolidus are available for natural pyroxene compositions. In the laboratory, Ross and Huebner (1975, 1979) converted natural orthopyroxene + augite to pigeonite. Their experiments constrain the O + A $\rightleftarrows$ P equilibrium to lying at or below a line connecting the following values of temperature (°C) and Fe/(Mg + Fe): 1270° and 0.08; 1102° and 0.46. At more iron-rich compositions, augite was generally not present when pigeonite formed from orthopyroxene. In this region, the reaction of orthopyroxene + augite to form pigeonite must lie below a line connecting the points 1102° and 0.46; 900° and 0.86. For very iron-rich bulk compositions, the stability limits of assemblages can be gleaned from reports of the occurrence of orthopyroxene, pigeonite, augite, olivine, and silica in iron formations (Bonnichsen, 1969; Simmons *et al.*, 1974), and of evidence that ferrobustamite was a late-stage fractionation product of the Skaergaard intrusion (Brown and Vincent, 1963). Because knowledge of the pyroxene subsolidus is derived largely from natural materials, we defer diagrams that attempt to portray such relations until we discuss the phase relations of natural pyroxenes in the next section. However, it is worth emphasizing at this point that because we do not think that additional minor components such as Al_2O_3 and TiO_2 will greatly affect the pyroxene subsolidus, we model the subsolidus for pure pyroxenes after the subsolidus deduced from natural pyroxenes. Despite some uncertainties in earlier work on the subsolidus, we are confident that in the pure system the pigeonite field

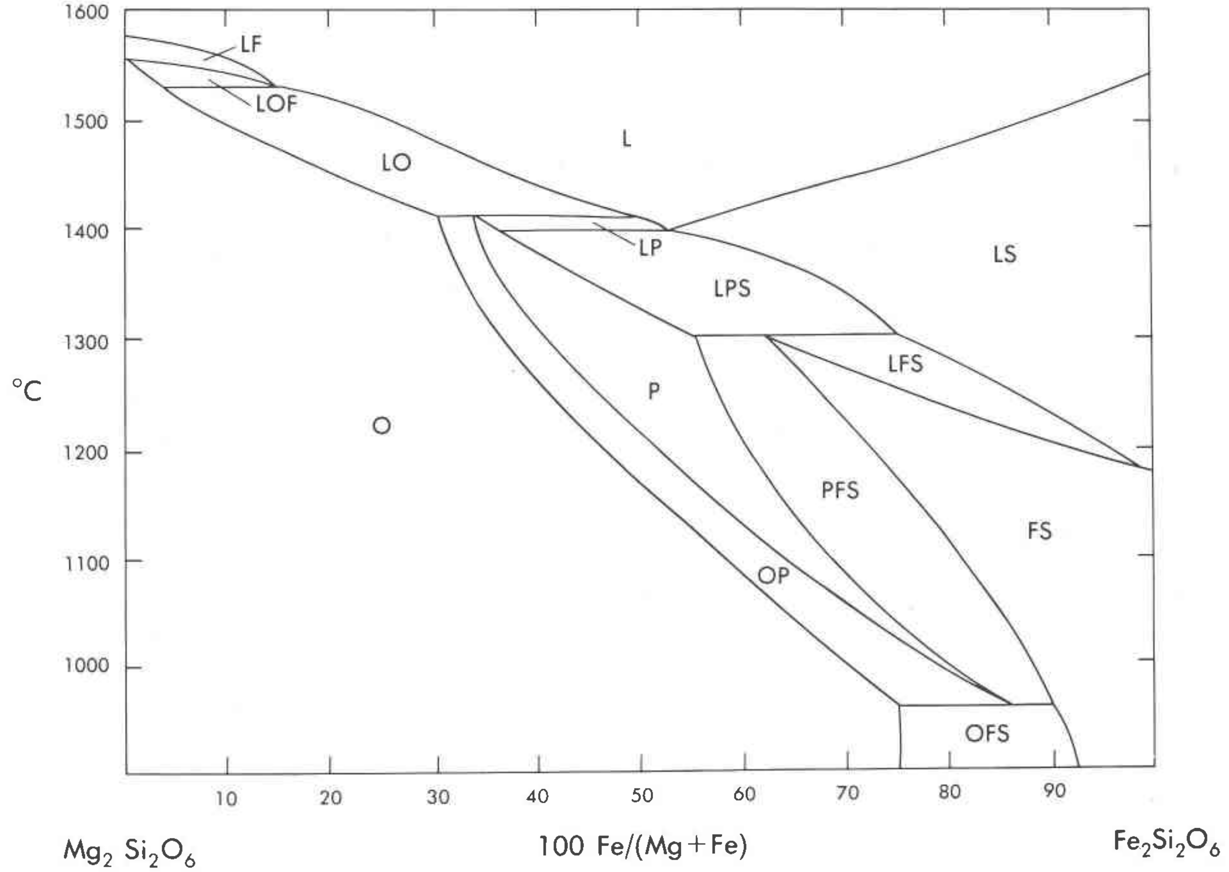

Fig. 6. *T–X* section along the En–Fs join, drawn from Figs. 4 and 5. This diagram revises that of Bowen and Schairer (1935; Fig. 8) by bringing the cotectic L(O,P) to the En–Fs join, thereby permitting orthopyroxene on the solidus for Mg-rich, Ca-free compositions.

extends to the iron-free join at temperatures close to the solidus.

Revised diagram, system $MgSiO_3$–$FeSiO_3$

It is possible to revise the phase diagram for the system $MgSiO_3$–$FeSiO_3$ (Bowen and Schairer, 1935, their Fig. 8) to reflect the fact that orthopyroxene is present at the solidus at Fe/(Mg + Fe) < 0.3 (Figs. 4 and 5, this paper). The revised diagram, our Figure 6, helps emphasize the fact that the solidus position is extremely sensitive to the amount of calcium present where the calcium concentration is small. At Fe/(Mg + Fe) = 0.50, the solidus temperature ranges from 1330°C at Wo = 0 (Fig. 6) to 1220°C at Wo = 12 (Fig. 4b).

III. Melting relations of natural pyroxenes

As part of a comprehensive investigation of the phase relations of naturally occurring pyroxenes, one of us (JSH) extended previously reported studies on the subsolidus relations into the melting region. Rock-forming pyroxenes invariably contain minor components such as Al_2O_3, Cr_2O_3, MnO, Na_2O, and TiO_2, in addition to the major or quadrilateral components CaO, MgO, FeO, and SiO_2 that were discussed previously. In this section we will examine the melting relations of natural pyroxenes containing minor components ("others"), principally Al_2O_3 and TiO_2, and discuss the effects of the minor components on pyroxene phase relations.

Experimental techniques utilizing natural pyroxenes

Our technique utilized single crystals of pyroxene separated from igneous and metamorphic rocks of terrestrial and lunar origin. Although use of minute single crystals has the disadvantage of making laboratory manipulation difficult and examination by conventional X-ray powder diffraction methods impossible, it offers advantages over conventional techniques in which synthetic materials are used. Both the starting material and the residual pyroxene can be characterized by X-ray precession photography.

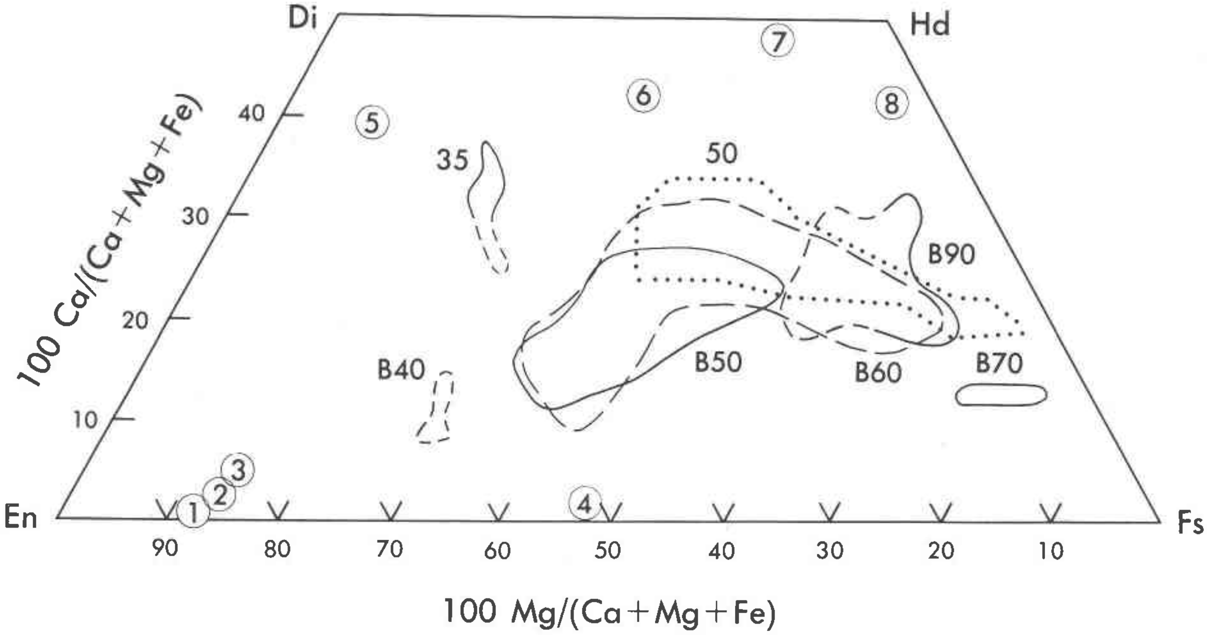

Fig. 7. Projection onto the pyroxene quadrilateral of the compositions of the lunar and terrestrial pyroxenes used in the partial melting experiments. Numbered circles 1–8 refer to terrestrial pyroxenes: 1, NMNH-82436; 2, J-8; 3, 61SC-B; 4, 223 OPx; 5, 61SC-A; 6, 17a-CPx; 7, PO-17-A; 8, M-12330. Complete chemical analyses of these terrestrial pyroxenes are given in Table 2. The fields between Wo 7 and 38 percent refer to pyroxene separates from the lunar basalt 12021 described by Ross *et al.* (1973). Six of these separates were analyzed with a microprobe by Huebner and Hickling. The chemical analyses on which the position of pyroxferroite separate B70 is based are from Boyd and Smith (1971).

Both the reactant and the products are of sufficient grain size for good microprobe chemical analyses, even for runs made at < 1100°C. We selected pyroxene crystals from 8 homogeneous separates of terrestrial pyroxenes (Table 2[2] and Fig. 7) and from 7 separates of lunar pyroxenes (Fig. 7). This small number of bulk compositions adequately covers the compositional range of most rock-forming, quadrilateral pyroxenes. Most (14) of these pyroxenes have been studied and reported previously; we believe that their chemistry and mineralogy are unusually well documented.

Pyroxene single crystals (100–1000 micrometers) were heated at 1 bar in a controlled-atmosphere, gas-flow furnace. The samples were contained in iron or platinum–iron alloy foil envelopes (Huebner, 1973). The alloy was prepared at ~ 1000°C in evacuated silica tubes by permitting platinum foil to dissolve iron from the "vapor" generated by iron powder or granules. Other details of the experimental method and the examination of the run products are given by Huebner *et al.* (1976; method 1). We adequately maintained the bulk composition of the sample during the run, despite the fact that the mass of the foil container greatly exceeded that of the charge.

Microprobe procedures and the test analyses of standards have been described previously (Huebner *et al.*, 1976). Most of the element weight percent values reported in Table 3[2] were determined using 13 mineral standards, as follows: Adirondack diopside for Si, Mg, and Ca (National Museum of Natural History #117733; William Melson, donor); jadeite for Si, Al, and Na (Coleman and Clark, 1968, analysis R-1854); Kakanui augite for Na, Al, and Si (Mason and Allen, 1973; Brian Mason, donor); Marjalahti olivine for Mg (Yoder and Sahama, 1957; William Melson, donor); sphene for Ti (Hemet Quadrangle, Oregon; U. S. Geological Survey analysis by E. Lillie, dated October 28, 1969, for David Gottfried); Tiburon albite for Al and Na (Crawford, 1966; David B. Stewart, donor); synthetic fayalite for Fe (synthesized by Huebner); Broken Hill rhodonite for Mn (NMNH #90102; analysis by J. J. Fahey of the U. S. Geological Survey for Huebner); hedenbergite for Mn and Mg (Bonnichsen, 1969, analysis #330, p. 223; Paul Weiblen, donor); synthetic lunar glass CG-77135 (Minkin *et al.*, 1976; Jean A. Minkin,

---

[2] To receive a copy of Tables 2 and 3, order document AM-80-131 from the Business Office, Mineralogical Society of America, 2000 Florida Avenue, NW, Washington, D. C. 20009. Please remit $1.00 in advance for the microfiche.

donor); and three standards for chromium as discussed in Huebner *et al.* (1976).

Coexisting crystals and glass were first analyzed with the same standards, a procedure chosen to obtain reliable data on minor-element partitioning. Were different standards used routinely for crystals and glass, specifically glass standards for our product glasses (as was done for some analyses performed in 1976), the glass analyses might total as much as three weight percent more, but this higher total would be achieved at the expense of confidence in the degree of element partitioning. In this regard, we note the results of the interlaboratory comparison of glass analyses by Jarosewich *et al.* (1979). This group found a surprisingly large degree of scatter in some minor-element (< 3 percent by weight) analyses.

Experimental results for 25 runs, spanning the temperature range 1300° to 1052°C, are reported in Table 3. In most runs, the foil envelope contained several pyroxene crystals; these crystals usually gave similar results. In each reported experiment, the silicon concentration of the liquid was sufficiently large to stabilize a pyroxene; 46 of the 52 liquid analyses have > 1.86 Si cations per six-oxygen formula unit. (The relationship between the concentration of silicon, expressed as cations per 6-oxygen formula unit, and the olivine–pyroxene field boundary is outlined by Huebner, 1975.)

Retention of bulk composition

Three criteria were used to decide whether or not the bulk composition was retained satisfactorily close to the metasilicate plane. (1) In compositional projection onto the pyroxene quadrilateral, the tie-line or tie-triangle of the product assemblage must pass close to or enclose the initial bulk composition. (2) The glass analysis, expressed in atomic proportions, should have a cation sum close to 4 cations per 6-oxygen formula unit. (If the charge acquired iron as FeO from the container, or precipitated silica, the sum should exceed 4.00 cations. If the charge lost iron as FeO, or precipitated olivine, the sum should be less than 4.00 cations.) In practice, we accepted glass analyses that had a cation sum greater than 3.80; 62 percent of the analyses had sums between 3.90 and 4.04. On the basis of analyses of the crystalline phases equilibrated under conditions at which iron should be predominantly Fe^{2+} (and some chromium Cr^{2+}), our microprobe technique yields cation sums that are usually within ±0.01 cations (always within ±0.03 cations) of the stoichiometric values (4.000 cations per 6-oxygen formula unit in pyroxene; 4.500 in olivine). For a number of runs we include analyses with poor cation sums. In each of these runs, however, we also present a "good" analysis of the phase. We did not delete the inferior analyses because they help give a clear picture of the difficulties we encountered in analyzing the fine-grained run products. The symbols plotted in Figure 10 enclose both the "good" and the inferior analyses; thus, the relative proportions of Ca, Mg, and Fe do not appear sensitive to analysis quality judged by cation sum. We tentatively assign a generous analytical uncertainty of ±0.05 cations to the glass analyses made at the same time as the crystal analyses. (3) In the glasses the number of silicon cations per 6-oxygen formula unit must be a "reasonable" value, nominally close to the value in the starting material (1.85–1.99). If there was fractionation of minor elements into the liquid and possible precipitation of silica, the value should be less than that of the starting material. Precipitation of olivine (which has close to 1.50 silicon cations per 6-oxygen formula unit) tends to increase the value. Drastic departures from the initial value could be caused by loss of iron from the charge (tending to increase the silicon concentration of the liquid) or uptake of iron (tending to decrease the value). We estimate that in each of the reported runs the bulk iron content of the charge was maintained close to that of the initial pyroxene.

Description of run products

Run products formed crystals and melt bodies of sufficient size for conventional optical microscopy and electron microprobe analysis. Photographs of representative polished grain mounts of the partially melted grains are shown in Figure 8. Melting is commonly initiated throughout the pyroxene grain (Fig. 8a), presumably at defects or inclusions; rarely, melting is clearly associated with exsolution lamellae (Ross and Huebner, 1979, Fig. 8). As the degree of melting increases, liquid segregates into a small number of larger masses within a crystal (Fig. 8b,c) or between grains (Fig. 8a). When melting is extensive, the crystalline run products are completely enveloped by liquid (Fig. 8d,h). Recrystallized pyroxene is clear and idiomorphic where in contact with melt (Fig. 8c,f). Cloudy pyroxene (Fig. 8a,f) is distinguished chemically from clear pyroxene by its relatively large content of alumina. The partial melting process results in an increased internal perfection of the pyroxene crystal; melt tends with time to migrate into masses of increasing size. The cloudy, aluminous pyroxene is probably a fine-scale intergrowth of tiny melt blebs and residual (refractory) pyroxene that cannot be distinguished by use of routine optical microscopy or electron microprobe techniques.

Solid phases adopt characteristic habits. Silica is invariably euhedral, forming laths (Fig. 8c,e). Olivine adopts its crystal form, but with rounded faces, in contact with melt or pyroxene (Fig. 8d,g). Pyroxenes sometimes form euhedral faces in contact with melt (Fig. 8f), as mentioned previously. Bustamite is usually anhedral or nearly so, even in contact with liquid (Fig. 8g).

Product phases were homogeneous within the statistical uncertainties of microprobe analysis. Composition gradients were sought in large crystals and bodies of liquid, but were not found. Likewise, different product crystals of the same phase (for example, the olivine crystals in Fig. 8d) formed from one single crystal of reactant had the same composition. The microprobe chemical analyses in Table 3 are averages of several analysis points in several areas or several accessible grains of each product phase. Analyses that appeared to represent mixtures of phases, a problem where tiny volumes are analyzed (*i.e.*, glass in Figs. 8a,b), were rejected before averages were computed.

Attainment of equilibrium

Experiments reported in this study are prograde melting experiments and thus do not demonstrate, by themselves, thermodynamic equilibrium by reversal of reactions. In our experiments, a homogeneous single phase is replaced by an assemblage of compositionally distinct phases, or an initial two-pyroxene intergrowth (augite + pigeonite in lunar basalt 12021) is replaced by an assemblage, the phases of which are compositionally more divergent than those in the starting material. Strictly speaking, we would expect that the tie-lines present in equilibrium assemblages are as long or longer than the tie-lines observed in our experiments. Practically speaking, we observed a situation that was stable with time, and we did not observe any violation of criteria that are necessary consequences of equilibrium: (1) Product phases are chemically homogeneous. (2) The experimental result is independent of the starting material used and the duration of the experiment. (3) Experimental charges tend to approach a textural equilibrium of euhedral crystals in melt (Fig. 8), but bustamite crystals in liquid (Fig. 8h) are an exception. (4) Where a comparison is possible our prograde melting experiments yield results that are similar to crystallization processes observed in the laboratory or deduced from igneous and volcanic rocks. (5) Our experimental results are consistent with our knowledge of mineralogical crystal chemistry. (6) The results are reproducible. (7) Our results are consistent with the phase rule.

Rigorous laboratory reversal of the partial melting process is an elusive goal, exceedingly difficult and rarely achieved. At best the experimentalist can convert crystalline material to melt (and *vice versa*), taking care to recognize that entirely different non-equilibrium processes may constitute the best "reversal" that can be obtained. Our partial melting process involves the formation of one solution (melt) from another (crystalline pyroxene). Were the temperature raised sufficiently slowly, the pyroxene could partially melt under close to equilibrium conditions. The proportion of liquid would change to maintain an equilibrium state of elemental partitioning. Such an equilibrium approach is not standard laboratory practice because of difficulties in coordinating the f_{O_2} values with temperature and in maintaining sample bulk composition for runs of long duration.

Like most other investigators, we placed the charge in the furnace so that it reached its final temperature of equilibration within several seconds. This final temperature is appreciably above the temperature at which melting would be initiated under equilibrium conditions. Melting must have been rapid, but we have no idea whether or not the compositional evolution of the liquid (and the crystal) with time was similar to the equilibrium case. We hope we achieved an equilibrium final state by the use of experiments of long duration—a duration sufficient, in most runs, to cause complete expulsion of the melt from the residual crystal (and consequent recrystallization of the pyroxene). As previously discussed, we found no evidence of disequilibrium.

Other investigators have used different starting materials (Table 4): polycrystalline rock powder, glass, devitrified glass, and gels. Most starting materials were placed in a furnace at its final equilibration temperature. This approach leads to the same uncertainties that plague our partial-melting experiments. Approach to the final state is by a succession of disequilibrium states, as crystallization proceeds isothermally. Several runs were initially heated above the desired temperature, then quickly reduced to the desired value. Approach to equilibrium from an initially higher temperature poses additional uncertainty if there is precipitation on cooling. Sufficiently long crystallization experiments reach a stable state and, with luck, may reach true equilibrium.

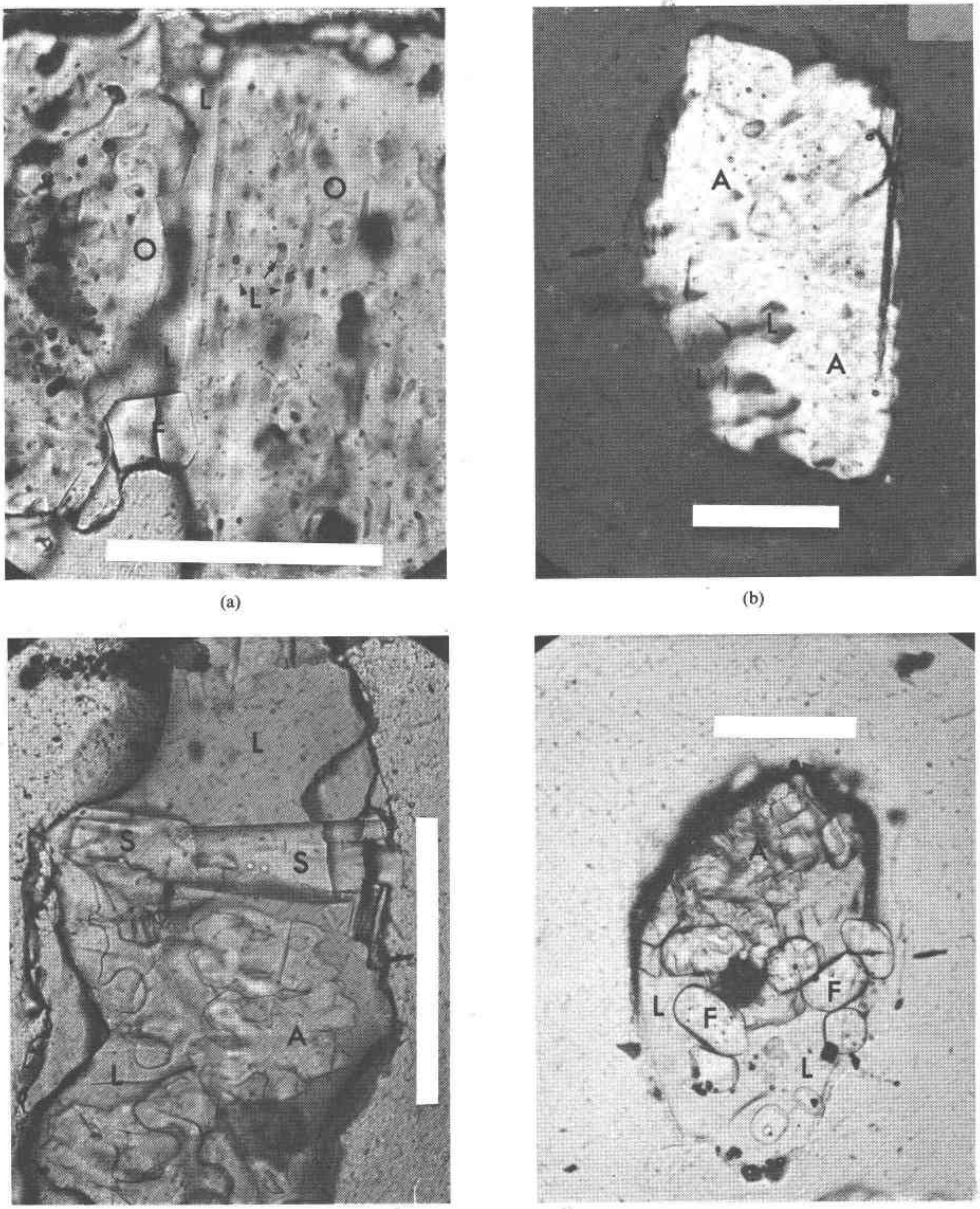

(a)

(b)

(c)

(d)

Fig. 8. Photomicrographs of representative run products illustrating the variety of textures observed in the experiments. The bar scale represents 100 micrometers in each photograph. Phases are abbreviated L(liquid), O(orthopyroxene), P(pigeonite), A(augite), F(olivine), B(bustamite), and S(silica). All runs are described in Table 3; photographs are discussed in text. 8a, 61SC-B, 1300°C; ordinary light. 8b, Ca-17a-CPx, 1178°C; ordinary light. 8c, 12021,B90, 1102°C; ordinary light. 8d, 12021,35, 1208°C; ordinary light. 8e, 12021,B90, 1102°C; ordinary light. 8f, 61SC-A, 1273°C; ordinary light. 8g, 223, 1226°C; inclined nicols. 8h, Po-17, 1077°C; inclined nicols.

Fig. 8. (continued)

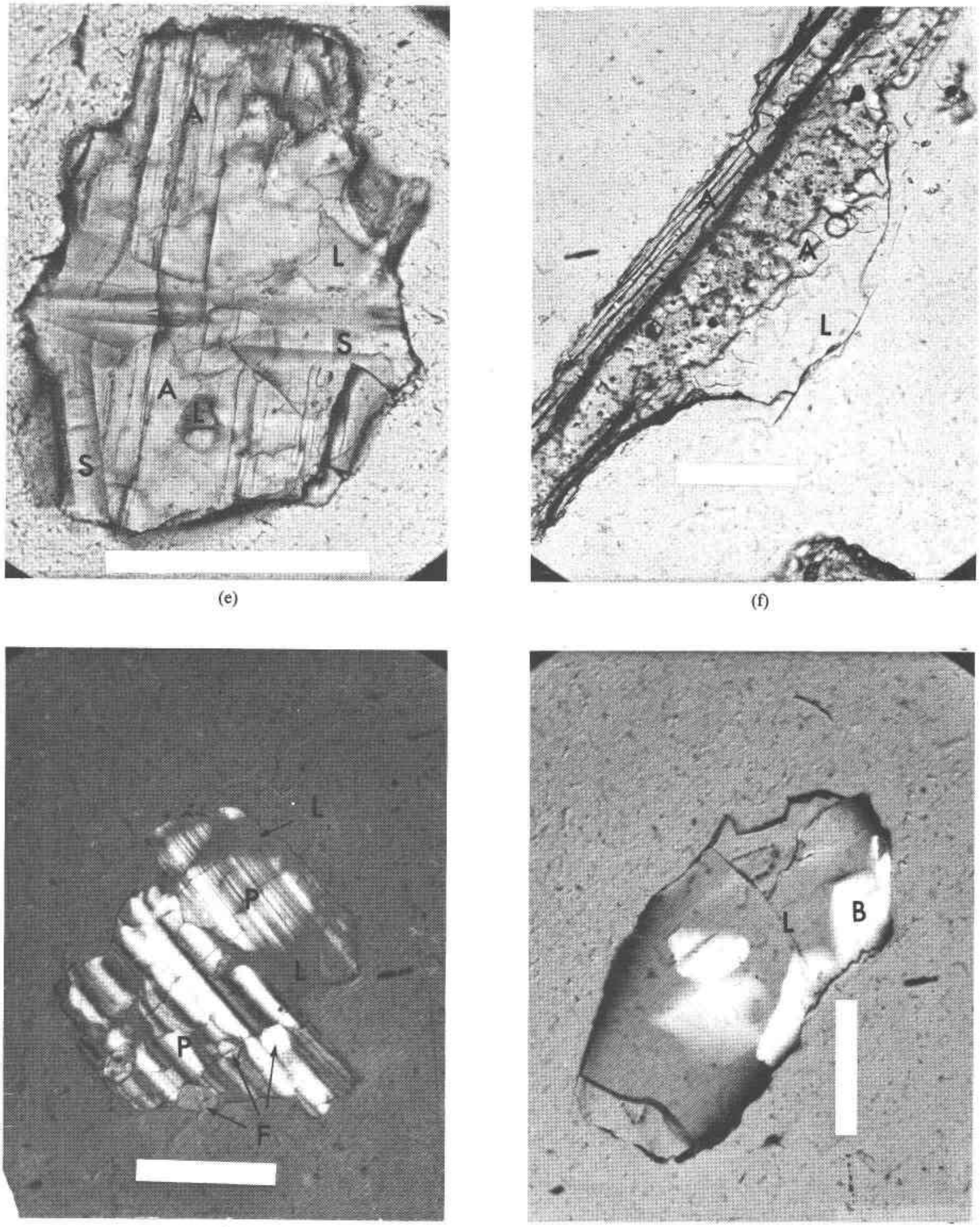

(e)

(f)

(g)

(h)

Table 4. Summary of related investigations

Reference	Bulk Comp 1/	Phases	T°C	Reactants 2/	Comparison with this report 3/				
					Ca-Fe-Mg tie line compatibility	Similarity of 1/D value			
						Al	Ti	Cr	Mn
Biggar et al. (1971)	12038 LTMB	LP, LPF	1137, 1114	GR, Gel	=	<	=	<	=
	12064 LTMB	LP, LPA	1160, 1114	GR, Gel	=	<	=	<	=
	12040 LTMB	LPAF	1137	GR, Gel	=	<	=	<	=
Longhi et al. (1974)	70017 HTMB	LPA, LA	1134, 1126	GR, PPR	=	=	=		
Walker et al. (1976)	12002 LTMB	LPF	1176-1150	DGl	=	=	=	=	=
Grove & Bence (1977)	Residual melt of 11597	LP	1194-1123	Gl	=	=	=	=	=
Longhi (personal communication, 1978)	MKB7-1	LP	1196	DGl	=	=	=	<<	
Akella and Boyd (1973)		LO	1160	1	≠	<	<		
			1130-1110	1	=	<	=		
Weill and McKay (1975a)	VHA basalt	LP	1200	?	=	<	<	=	
O'Hara et al. (1974)	10017 HTMB	LA	1108	?	≠	<	<	<<	=
	10020	LPA	1133	?	≠	=	=	<	
	10062	LAF	1120	?	=	<	<	<<	
Weill and McKay (1975b)	FMG	LOF	1320-1220	?	≠	=	=	<	

1/ Five-digit number indicates a lunar basalt. LTMB and HTMB are low- and high-titanium mare basalts.

2/ Gl=glass, DGl=devitrified glass, GR=ground rock (lunar sample), PPR=product of a previous run, Gel=gels.

3/ > greater value of 1/D than in present investigation.
< smaller value of 1/D than in present investigation.

= approximately the same orientation and length, or value, found in the present investigation.
≠ not approximately the same orientation and length, or value, found in the present investigation.

It is tempting to conclude that our partial-melting experiments and the crystallization experiments of other groups bracket or reverse the elemental partitioning values. However, even if there were no differences in bulk composition, this conclusion would not be rigorously correct. The path by which crystal is converted to melt is not simply the reverse of the path by which melt becomes crystal. As will be shown later, other investigators, using a variety of starting materials, have achieved a final state that, in respect to elemental partitioning, is similar to the state we achieved in our experiments.

Phase diagrams for natural pyroxene compositions

Compositions of individual product phases were obtained by electron microprobe analysis (Table 3). The resulting phase diagrams emphasize the compositions of coexisting phases. The liquidus diagram (Fig. 9a) reflects the compositions of the generally small amounts of liquid that coexist with solids (plotted on the solidus, Fig. 9b), rather than the bulk composition which is the compositional datum for each run in the synthetic system. Thus, the melt compositions projected onto the liquidus do not have the bulk compositions of the starting materials. The technique is different from that described in Part II of this paper, in which the liquidus temperature was determined by observing a run with such a small amount of crystals that the liquid composition could be assumed to be the same as the bulk composition. The isothermal sections were drawn primarily from the liquidus and solidus diagrams and show tie-lines determined by experiment (Table 3).

To the greatest extent possible, we modelled the phase diagram for natural pyroxenes on the diagrams for synthetic pyroxene compositions. More complete data are available for the pure system, and fewer compositional variables are present to cause scatter or "noise" in the data. We assumed that additional, minor components would not alter the shapes or sizes

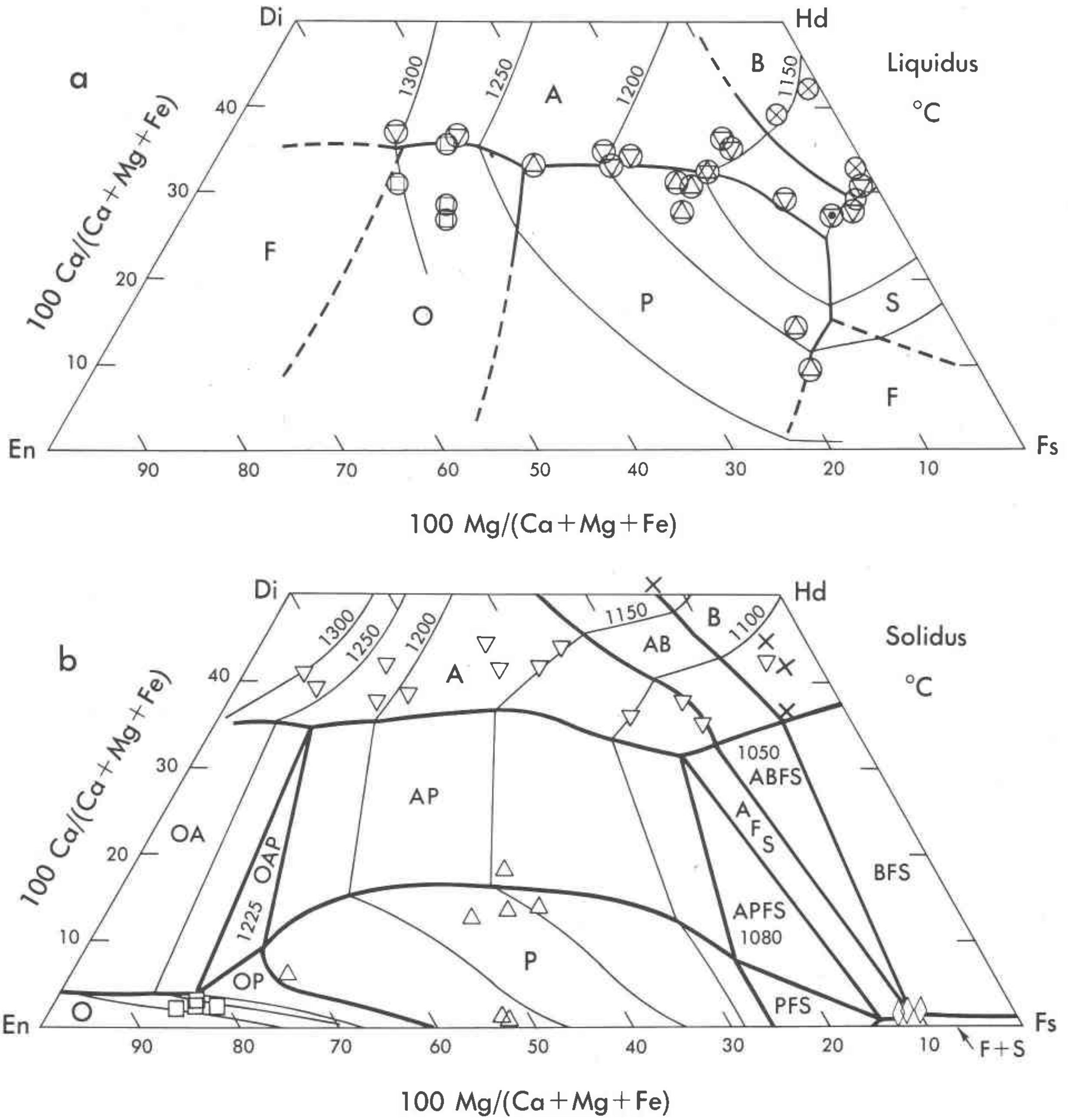

Fig. 9. Projections of the liquidus (a) and solidus (b) for natural pyroxenes, based upon experiments reported in Table 3. Plotted liquids are enriched, relative to crystalline phases, in the minor components Al_2O_3 and TiO_2; nevertheless, the melts are close to metasilicate composition (as discussed in the text). Symbols have the same meaning as used previously. The projection point for olivine and liquid is silica. The curves separating the fields of O, A, and F intersect at the point where the pseudoquaternary isobaric univariant curve L(O,A,F) pierces the pyroxene plane. Similarly, L(A,B,S), L(A,P,S), and L(P,F,S) are piercing points. The temperature is in °C.

of the phase volumes in the subsolidus. The solidus (Fig. 9b) could then be drawn by depressing the temperatures of the synthetic solidus (Fig. 4b) by amounts we determined from our experiments on natural pyroxenes (Table 3; Fig. 9). The liquidus for the natural system (Fig. 9a) was drawn to be consistent with the solidus, to account for the experimental data, and to reflect the fact that, compared to the pure system, the topology and positions of the piercing points will change as the liquidus temperature is lowered.

Analyzed melt compositions were projected (by normalizing so that the sum of the Ca, Mg, and Fe cations is 2.000) onto the pyroxene quadrilateral and the temperatures of the individual partial melting experiments were contoured to provide liquidus isotherms. Despite the fact that the melt compositions varied irregularly in terms of components that were not used in contouring (SiO_2, $Al_2Al_2O_6$, $M^{2+}TiAl_2^{IV}O_6$, $Mn_2Si_2O_6$, *etc.*), there were few inconsistencies, and such inconsistencies involved only temperature, not the identity of the liquidus phase. It was possible to draw isotherms that described most run temperatures with an uncertainty of less than 20°C. The few exceptions, one of which is inconsistent by 50°C, will be discussed later. The residual crystalline phases contained a great proportion of the quadrilateral components Wo, En, and Fs (and thus a small proportion of the minor components or "others"). The solidus could be contoured to ±10°C, that is, with greater precision than the liquidus. The only exceptions are two runs that are also inconsistent in the liquidus diagram.

The liquidus for natural pyroxenes, like that for the pure system, has a trough which extends, as temperature decreases, across the quadrilateral toward the hedenbergite–ferrosilite join. There are significant differences, however, with respect to temperature and topology. Liquidus isotherms in the natural pyroxene system (Fig. 9a) are lowered 50° (for magnesian augites) to 100°C (for iron-rich augites), relative to the pure pyroxene system (Fig. 4a). The piercing points L(A,B,S) and L(A,P,S) are displaced toward the $FeSiO_3$ composition, and a new piercing point, L(P,F,S) has appeared, as might be predicted from Figure 4c. Most important, the orthopyroxene field adjoins the augite field. Orthopyroxene + augite can coexist on the liquidus; pigeonite is restricted to liquids less magnesian than about Fe/(Mg + Fe) = 0.45.

The topology of the natural solidus (Fig. 9b) differs in one important respect from the solidus for the pure system: the pigeonite field does not reach the iron-free join, En–Di. The temperature range of the natural solidus has been lowered by an amount sufficient to cause the solidus to pass through the pigeonite field and expose the orthopyroxene + augite miscibility gap. In other respects, the natural solidus differs only in the position of fields and boundaries. The pigeonite + augite miscibility gap has widened, primarily at the expense of the augite field, as predicted from the diagrams of Ross *et al.* (1973, Fig. 9). The fields APFS and ABFS have moved toward the magnesium-free join, which is in accord with the results of Smith (1971, Fig. 3a) who showed that the calcium-free assemblage orthopyroxene + olivine + quartz becomes more iron-rich as temperature decreases. Although it is not closely constrained by experiment, we have displaced the field of augite + bustamite toward the magnesium-free join, as would be anticipated from our Figure 3e.

A series of isothermal sections for the natural pyroxene quadrilateral is shown in Figure 10. The compositions of coexisting phases for each of the runs reported in Table 3 are superimposed on the isothermal sections. The temperatures of the sections were chosen so that the experimental runs could be grouped together; for example, 1200°C was chosen for a section because that temperature value is midway between, and close to, actual run temperatures of 1208° and 1192°C. In only one case—involving runs at 1243° and 1242°—was the decision difficult; we found that the isothermal sections were internally more consistent if the 1243° run was shown on the 1250°C section, and the 1242° run shown on a section for 1230°C.

In general, the phase boundaries shown in the diagrams lie close to the projected compositions of phases. The observed degree of scatter or mismatch is reasonable if one considers the analytical uncertainties involved in analyzing the glasses, especially for MgO, and the fact that the projections onto the quadrilateral show only relative variations of Ca, Mg, and Fe, concealing the real variations in the other components. The only glaring experimental inconsistency is a run at 1126°C (Fig. 10): the tie-line between augite and melt is anomalously long, and the augite is anomalously calcic relative to the melt, causing conflicting tie-line orientation. This run does not fit well in either the 1100° or the 1140°C section, but has been included in the 1140° section because we have no rational basis for excluding it from our data set. However, this run did not influence our placement of field boundaries or sketching of tie-lines. The second problematical run, at 1123°C (Table 3) and plotted on the 1140°C isotherm (Fig. 10), has a reasonably oriented but anomalously long tie-line between liquid and pigeonite. This is the previously mentioned run that does not agree with the solidus and liquidus isotherms. Again, we include this run because we have no objective basis, such as faulty experimental procedure or bad microprobe analyses, for excluding it from the data set.

Low-calcium pigeonite

We presented earlier (Fig. 9b) the interpretation of the pigeonite field which best fits our experimental data. The pigeonite field forms a gently sloping plateau on the solidus, and orthopyroxene of composition Fe/(Mg + Fe) $\gtrsim$ 0.15 is thus prevented from coexisting with augite on the solidus. We show the field OP approaching more magnesian compositions as temperature descends, and place the quasi-peritectic reaction point L(O,P,A) at 1225°C. This topology permits the solidus to remain at ~1200°C in the region of calcium-poor, intermediate pigeonite ($Wo_1En_{53}Fs_{46}$). The topology also provides the steep orthopyroxene solidus surface required for two runs described by Ross and Huebner (1975, 1979) and found in the pure system (Fig. 4b).

The position of the assemblage OPA on the solidus is not invariant. We place it at Fe/(Mg + Fe) ~ 0.18, in agreement with our data, but at more magnesian bulk compositions than observed in the Bushveld intrusion [Fe/(Mg + Fe) ~ 0.35; Atkins, 1969] and in other gabbroic intrusive rocks. Ross and Huebner (1975) found that partial melting accompanies the transformation of some natural orthopyroxene + augite intergrowths to pigeonite over a range of Fe/(Mg + Fe) = 0.43 to 0.12 (and a corresponding temperature range of 1080° to 1270°C). We believe this widely ranging and seemingly variable position in terms of Fe/(Mg + Fe) of the assemblage OPA on the solidus is caused by the variety of bulk compositions under consideration. For each composition (and pressure) there is a different temperature at which the solidus intersects the pigeonite volume. In the pure synthetic system, solidus temperatures are high and the pigeonite volume reaches the En–Di join, permitting iron-free pigeonite to be stable along that join (Fig. 11, T_4). As minor elements are added to the system, the solidus temperatures are depressed and the solidus moves downward, cutting across the pigeonite field. When the solidus lies at ~ 1300°C at $Wo_9En_{91}Fs_0$, iron-free pigeonite is no longer stable (Fig. 11, T_3), and a three-phase triangle OPA appears on the solidus (Fig. 11, T_2). As the solidus is further depressed, the field OPA moves toward progressively more iron-rich compositions. The observed position of the OPA field depends upon the relative position of the solidus: in relatively pure systems that have a high melting point, pigeonite can be very magnesian; in impure systems that have low solidus temperatures, pigeonite is confined to more iron-rich compositions.

The position of the OPA field is potentially a good geothermometer, as pointed out by Ross and Huebner (1975). The sensitivity of its position to changes in solidus temperatures is caused by the fact that the pigeonite phase volume is oriented at a slightly steeper angle than the solidus, as shown in Figure 12. (The T–X section is drawn along Wo = 15, a composition at which pigeonite can be in equilibrium with both orthopyroxene and augite.) In our natural system, the solidus (constructed from Figs. 9 and 10) is depressed ~100°C relative to the solidus in the pure pyroxene system (from Figs. 4 and 5). This depression is sufficient to erode the pigeonite field from the En–Di join to Fe/(Mg + Fe) = 0.22. In real magmas, where plagioclase is present, the solidus depression can exceed 100°C, as in the Bushveld intrusion example, where the pigeonite field is eroded 150°C, to Fe/(Mg + Fe) $\simeq$ 0.3. The apparent shift in position of the LOPA field is related to the different chemical systems or different minor-element concentrations being considered.

Minor element partitioning and depression of solidus

Preceding sections have examined the differences between the pure or synthetic system and the natural system containing minor elements. We have alluded to the idea that minor elements cause the observed depression of the liquidus and solidus temperatures and the consequent changes in phase topology, but we have not yet examined the supporting data. In this section we will discuss the behavior of minor elements during the partial melting process and evaluate the effects that such partitioning might have on the phase diagrams. We will defer quantitative discussion of the thermodynamic aspects of such partitioning for a future paper on the quaternary phase relations; such thermodynamic discussion is not necessary for construction of the phase diagrams.

All chemical partitioning will be expressed in terms of the reciprocal of the partition coefficient of the appropriate oxide, 1/D (where D equals weight percent of oxide in crystals/weight percent oxide in melt). Use of the reciprocal of the conventional partition coefficient will emphasize the partitioning of minor elements into the liquid. When the concentration of an element is greater in the melt than in the coexisting crystals, values of 1/D will exceed unity. We have chosen weight percent ratios (1/D) rather than the reaction constant (K_D) because we do not know the speciation or the thermodynamic activities of the minor-element components in the crystals and the melt.

Examination of the chemical analyses in Table 3 reveals that Al_2O_3 is invariably enriched in the partial melt, relative to the crystals. Titanium, where initially present at levels suitable for routine microprobe analysis, is also found to be invariably enriched in the melt. Neither MnO nor Cr_2O_3 are strongly partitioned between pyroxene and melt. We

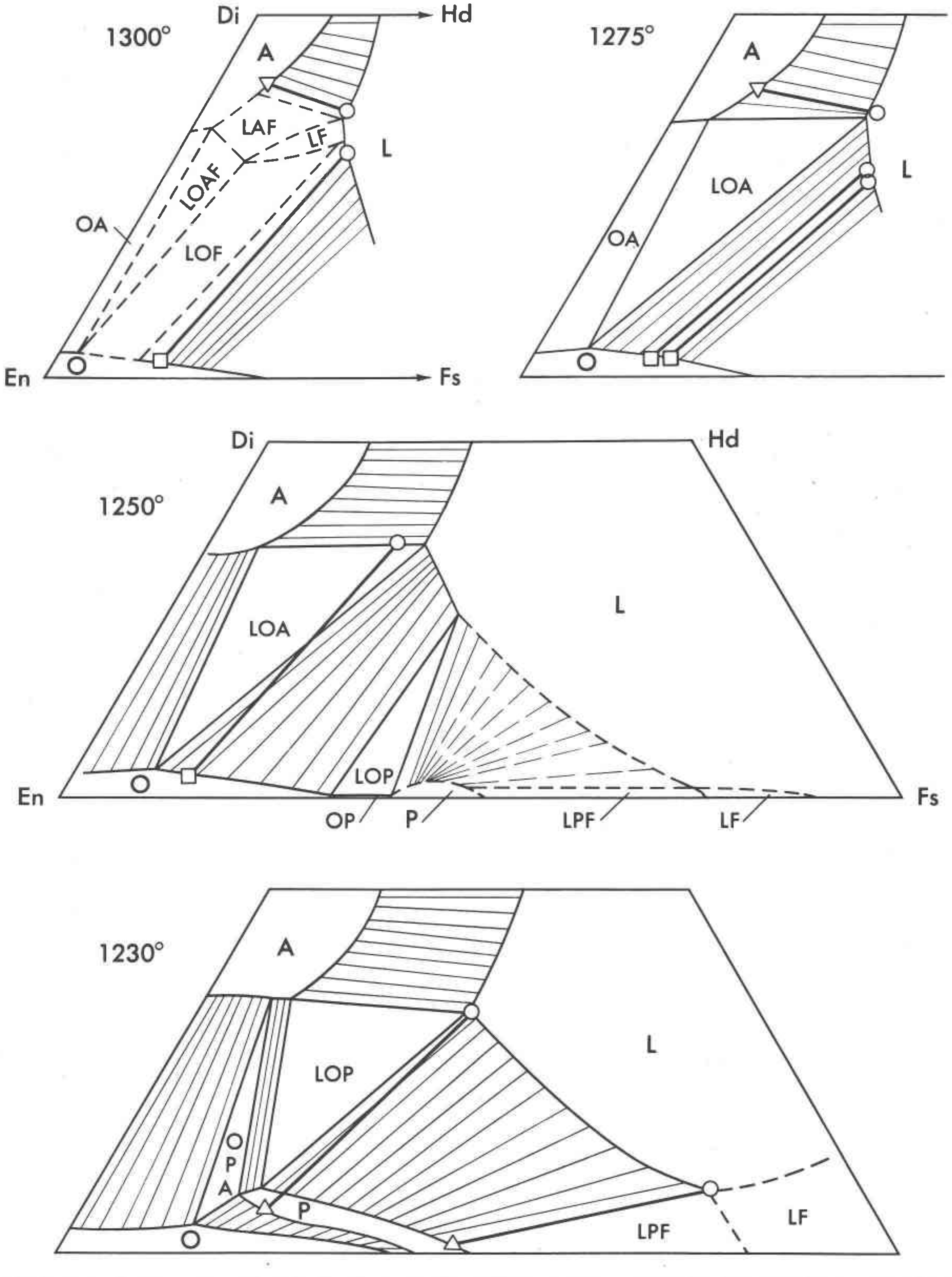

Fig. 10. Isothermal sections drawn from the liquidus and solidus of the natural pyroxene system (Fig. 9a,b) for the region in which melting occurred in our runs. Compositions of coexisting pyroxenes, olivines, and melt (Table 3) are projected onto the quadrilateral plane; symbols are the same as in Fig. 9. All temperatures are in °C. Heavy tie-lines are schematic. The subsolidus relations are not based upon experiment; rather, the section at 800–900° is sketched about the natural assemblage APFS (Simmons *et al.*, 1974) and the section at 700–800° is based upon the natural assemblage OAFS (Bonnichsen, 1969, samples 006 and 122).

Fig. 10. (continued)

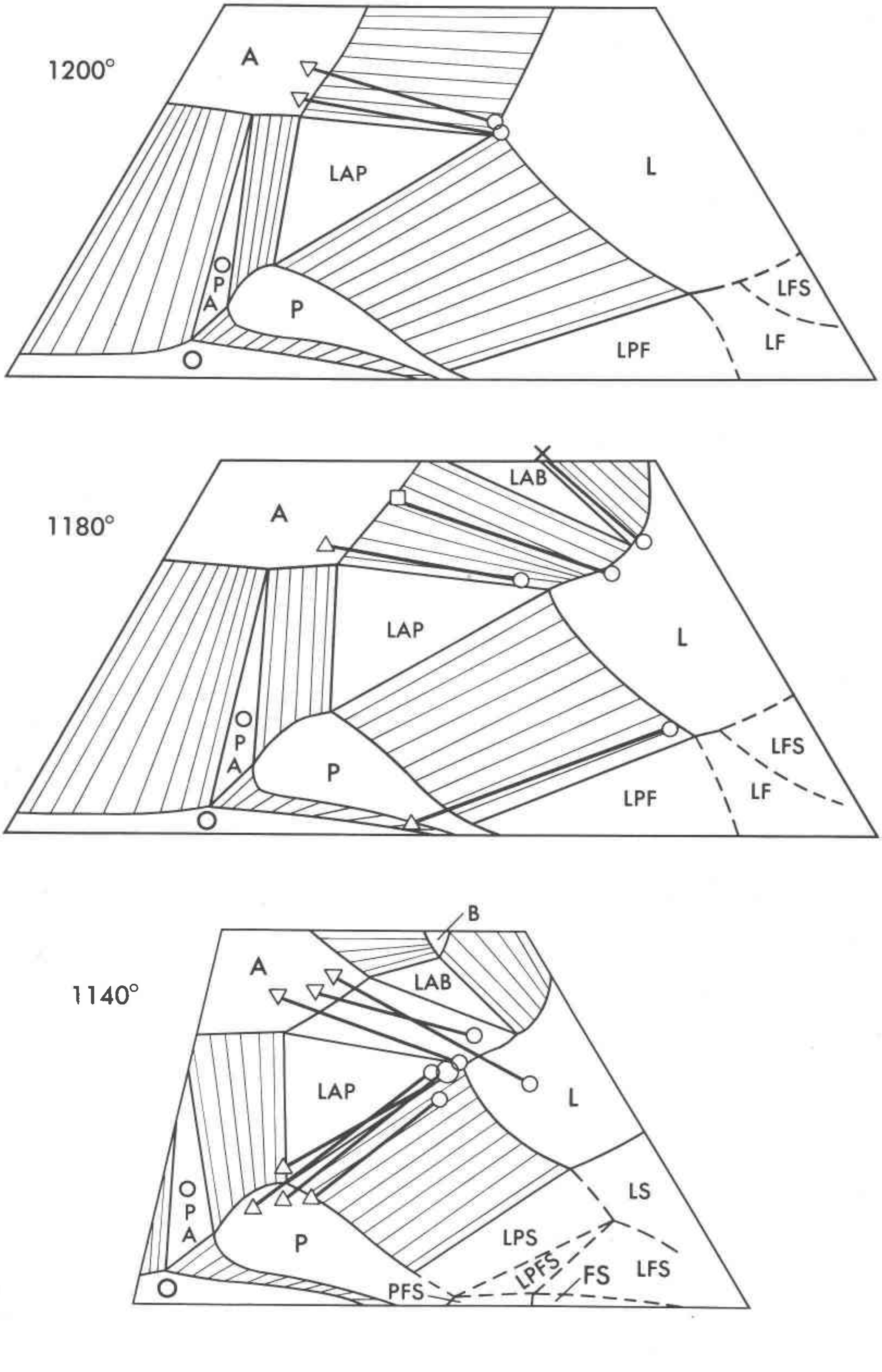

Fig. 10. (continued)

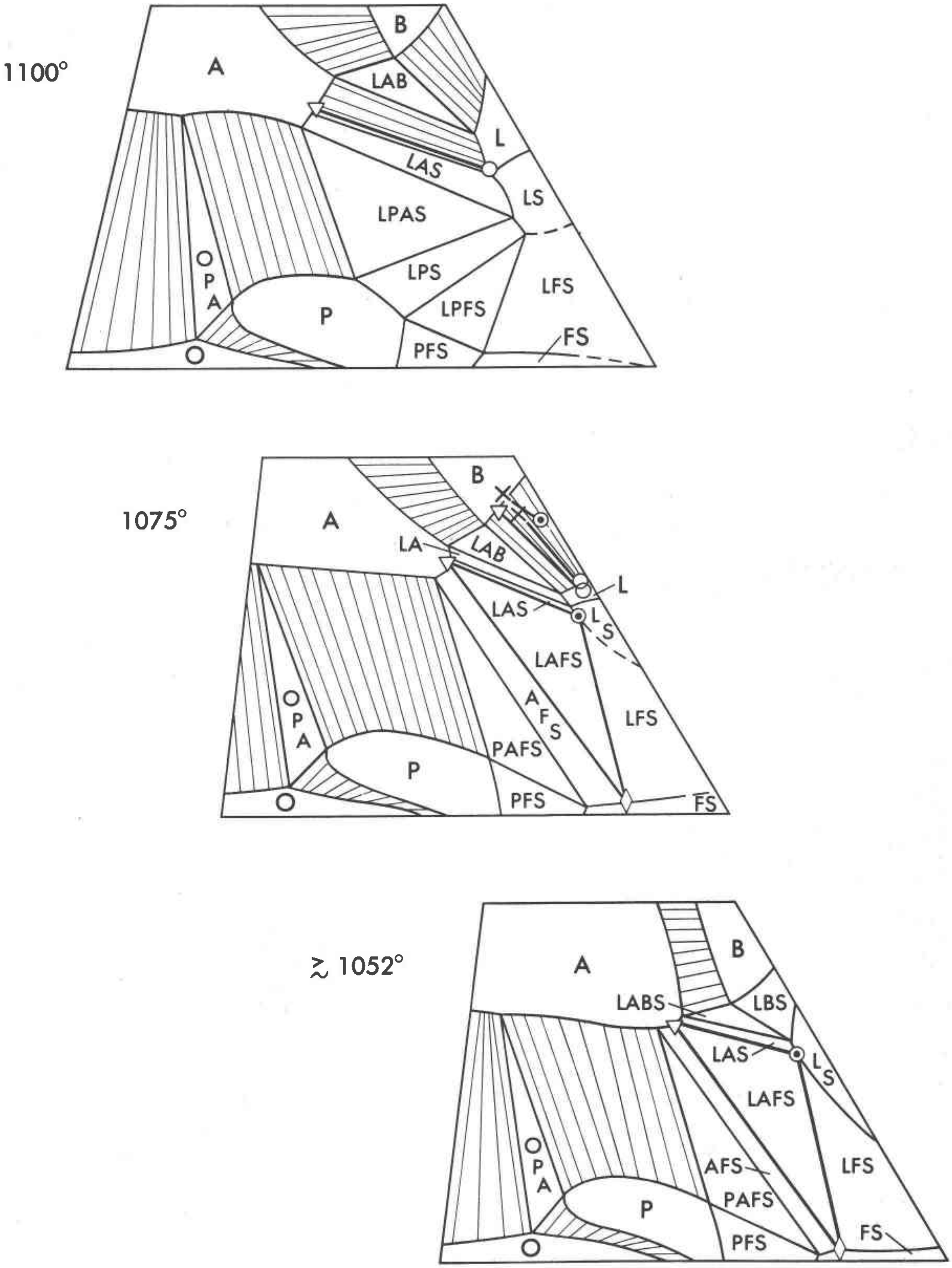

Fig. 10. (continued)

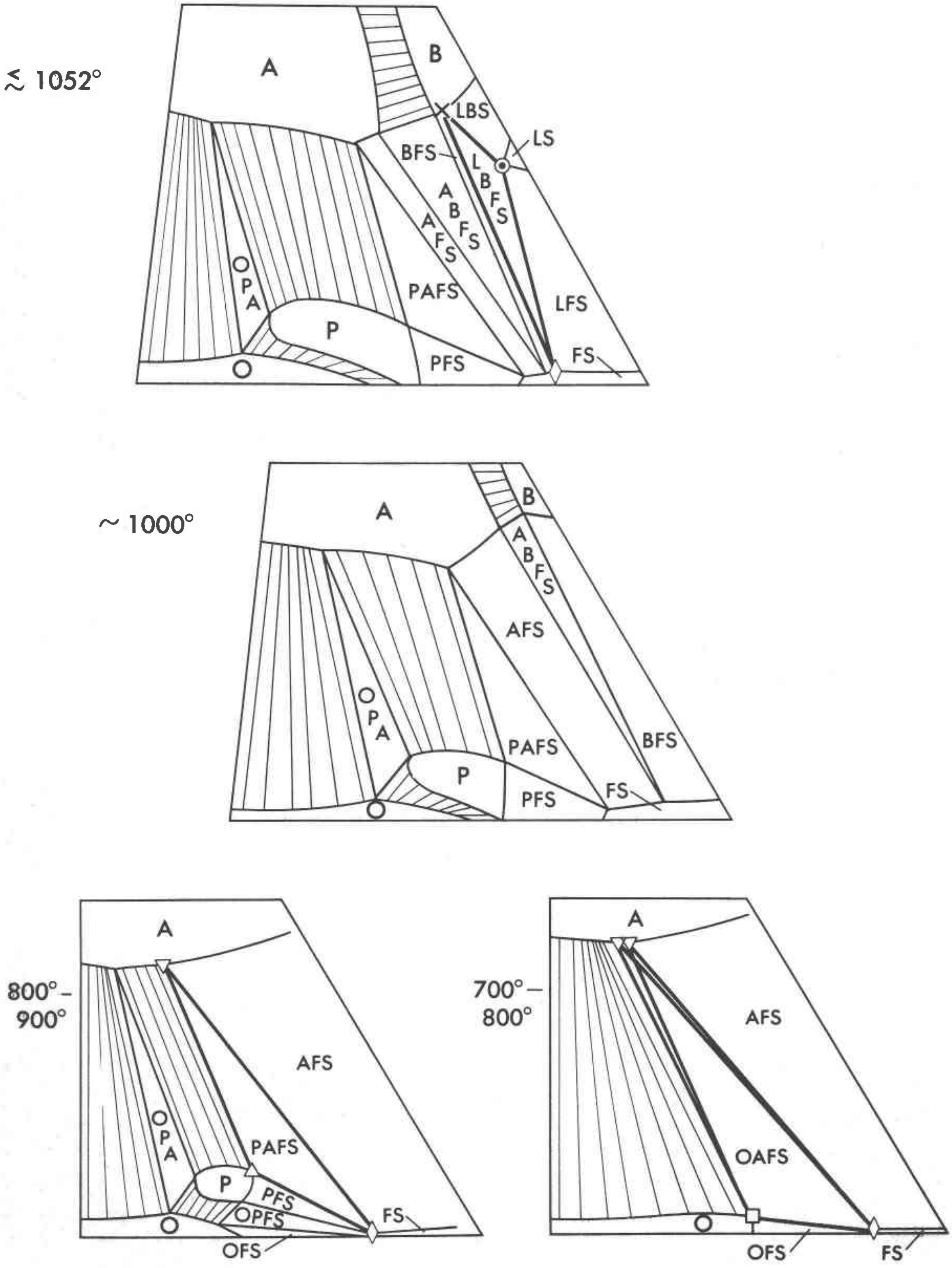

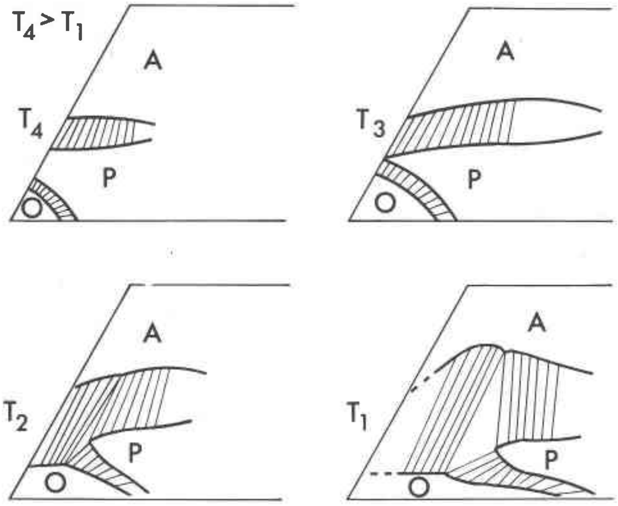

Fig. 11. Series of solidus surfaces illustrating the change in topology and extent of the pigeonite field as the solidus is lowered in temperature from that of the synthetic system $CaSiO_3$–$MgSiO_3$–$FeSiO_3$, T_4, through the solidus for the natural system, T_2, to the solidus for gabbroic magma such as that which formed the Bushveld Complex, T_1.

observe that Al_2O_3 and TiO_2 are present in sufficient quantities in some terrestrial pyroxenes (Table 2) and the lunar pyroxenes (Ross *et al.,* 1973) used in our experiments to become major constituents (as much as 11 percent Al_2O_3, 3.1 percent TiO_2 by weight) of the melt, thereby appreciably diluting the melt with respect to the simple pyroxene components $CaSiO_3$, $MgSiO_3$, and $FeSiO_3$. In this sense, our liquidus diagram (Fig. 9a) is valid for more aluminous and titaniferous bulk compositions than is our solidus diagram (Fig. 9b).

Minor-element data are summarized in Figure 13a–d. All three pyroxene phases tend to exclude Al_2O_3 and TiO_2 (that was initially present) on partial melting, and thereby enrich the residual crystals in the components $CaSiO_3$, $MgSiO_3$, and $FeSiO_3$. These three components taken together are obviously more dilute in the melt than the residual crystals. The three pyroxenes (O,P,A) cannot be distinguished from each other on the basis of the distribution coefficients for Al_2O_3, TiO_2, Cr_2O_3, or MnO. Any distinctive crystal-chemical effects are masked by analytical un-

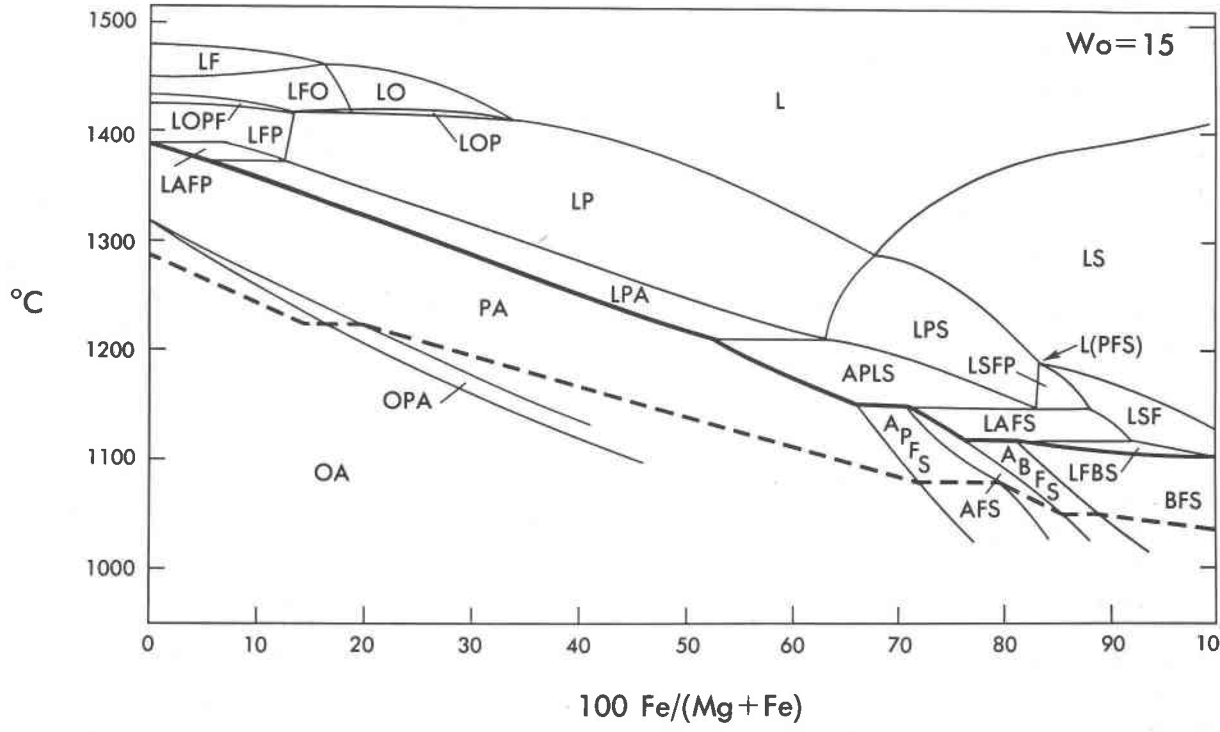

Fig. 12. Temperature-composition section drawn at constant Wo = 15 percent for synthetic pyroxenes (solid lines). The solidus (heavy line) passes above the orthopyroxene + augite ⇄ pigeonite transition, permitting stable, iron-free pigeonite to occur. In the dirty pyroxene system, the solidus (dashed line) lies beneath that of the pure system and intersects the orthopyroxene–augite–pigeonite transition (OPA). If we assume, as discussed in the text, that the subsolidus is insensitive to the presence or absence of minor elements, the figure shows how the position of OPA on the solidus is sensitive to minor changes in solidus temperatures.

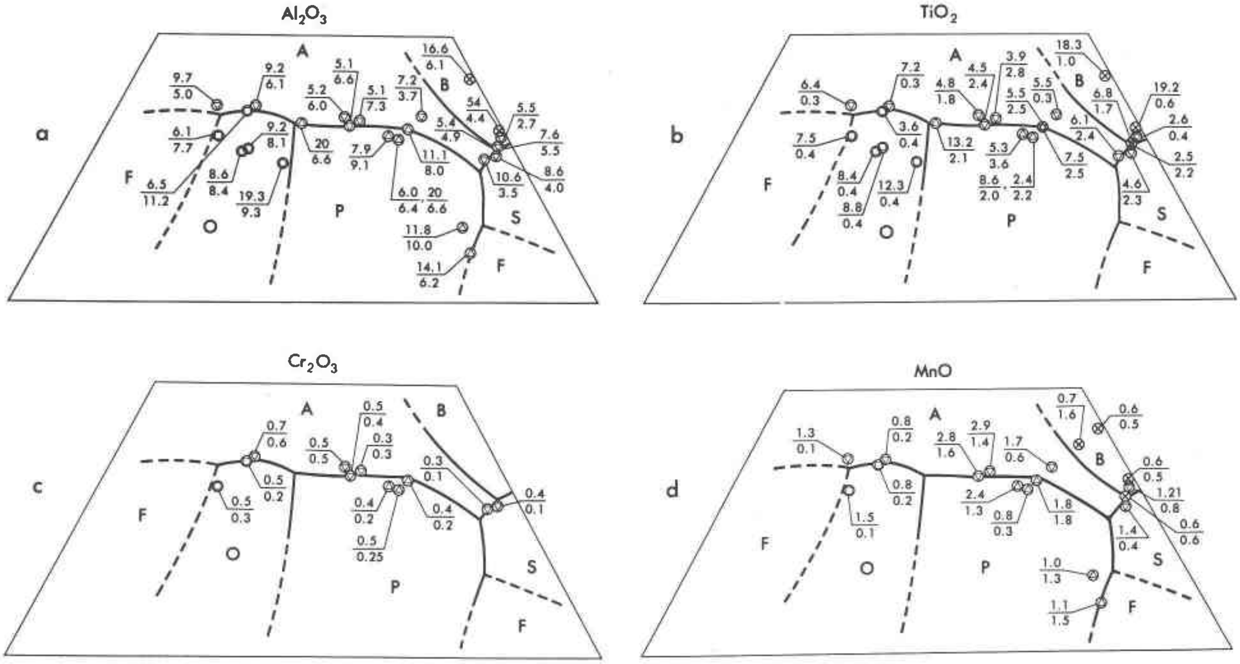

Fig. 13. Minor-element data projected onto the liquidus of the natural pyroxene system. The upper number associated with each run is the distribution coefficient ($1/D_{oxide}$), and thus shows the factor by which an element is enriched in the melt relative to the coexisting crystalline phase. The oxides Al_2O_3 (Fig. 13a) and TiO_2 (Fig. 13b) are always partitioned into the melt; Cr_2O_3 (Fig. 13c) is generally retained in the crystals during partial melting of pyroxene; and MnO (Fig. 13d) is not strongly partitioned. The lower number is the concentration of the minor element in the liquid, expressed as oxide weight percent.

certainties, differences in bulk composition, and the different run conditions (primarily temperature). The similarity of the values of $1/D$ for different pyroxene phases suggests that intrinsic differences between the distribution coefficients of the pyroxene phases are small. Ferrobustamite is distinct in excluding Al_2O_3 and TiO_2 more effectively than do the pyroxenes. In addition, the pyroxenoid tends to accept more MnO, relative to the liquid, than do the pyroxenes, particularly augite. This chemical distinction of ferrobustamite and augite proved useful in confirming the morphological distinction of two grains in the run involving the II-Po-17-Augite at 1077°C (Table 3).

The distribution coefficient for aluminum, $1/D_{Al}$, in pyroxene ranges from 5 to 20. Most (19 of 22) values in Figure 13a fall in the range 5 to 15; these 19 values average 8.2, with one standard deviation (σ) equal to 2.5 and one standard error of the mean ($\bar{\sigma}$) equal to 0.6. Values of $1/D_{Al} > 15$ may be real, but can also be attributed to analytical uncertainty and thus were not included in the average of 19 values. Had these three values been included, the average would have risen slightly (to 9.7), but the standard statistical parameters would have greatly increased (to $\sigma = 4.7$ and $\bar{\sigma} = 1.0$). Two runs with $1/D_{Al}$ equal to 3.3 (at 1126°) and 2.9 (at 1151°C) were neither plotted in Figure 13a nor included in the averages. We suspect that these two values reflect the observed incomplete separation of crystals and melt in runs at 1126° and 1151° (Table 3), which has caused the microprobe beam to excite both phases. We also excluded a value of $1/D_{Al}$ for augite of 4.9 at 1123°C because the augite was not immediately adjacent to the analyzed glass.

The average of 10 values of $1/D_{Al}$ for augite, 7.4 ($\sigma = 2.1$, $\bar{\sigma} = 0.6$) is smaller than the average of 9.9 for 5 orthopyroxenes ($\sigma = 5.4$, $\bar{\sigma} = 2.4$) or the average of 13.0 for 7 pigeonites ($\sigma = 5.5$, $\bar{\sigma} = 2.1$). This is somewhat surprising because we anticipated that clinopyroxene (both augite and pigeonite) would more readily accept Al_2O_3 than orthopyroxene at the low pressure of our experiments. However, the ranges of values for the three pyroxene data sets overlap to a large extent. The overlap is even more pronounced if values of $1/D_{Al} > 15$ are excluded from the averages.

Values of $1/D_{Ti}$ in pyroxene range from 2.4 to 13.2; the average of the complete data set of 21 observations is 6.2 ($\sigma = 2.9$ and $\bar{\sigma} = 0.6$). If the 5 values that lie outside the range 3.5 to 8.8 are excluded, the average is changed little (to 6.1), but the statistical uncertainty is significantly reduced ($\sigma = 1.7$ and $\bar{\sigma} = 0.4$). Values of 3.1 (at 1126°C) and 2.2 (at 1151°) were obtained from the same grains that gave anomalously low values of $1/D_{Al}$, and were neither plotted in Figure 13b nor considered in any averages for the reasons stated previously. The average of 11 determinations of $1/D_{Ti}$ for augite (4.9, with $\sigma = 1.5$ and $\bar{\sigma} = 0.4$) is distinctly smaller than that for 5 pigeonites (7.4 with $\sigma = 4.0$ and $\bar{\sigma} = 1.8$) and 5 orthopyroxenes (8.1 with $\sigma = 3.1$ and $\bar{\sigma} = 1.4$). Despite the considerable overlap of individual determinations in each of the data sets, augite appears to be a more favorable site for TiO_2 than is calcium-poor pyroxene (pigeonite or orthopyroxene). We recognize, however, that titanium enters pyroxene through a coupled substitution with another element, for example $M^{+2}TiAl_2^{IV}O_6$. For other bulk compositions, the substitution of titanium in pyroxene may be constrained by the abundance of other elements, particularly aluminum.

Values of $1/D_{Cr}$ for orthopyroxene, pigeonite, and augite are similar (Fig. 13c). Eleven measurements average 0.45 ($\sigma = 0.11$ and $\bar{\sigma} = 0.03$), in good agreement with the results of Huebner *et al.* (1976), whose data set includes some of the runs reported in Table 3. We excluded three measurements from our average. Values of 0.3 (at 1123°) and 0.5 (at 1126°C) are similar to our other determinations but were excluded because in the run at 1123° the analyzed augite was not immediately adjacent to the analyzed glass, and in the run at 1126°C the partial melt did not appear to be completely segregated from the residual augite. A third value of $1/D_{Cr}$ (1.4) falls outside the range of our data or those of Huebner *et al.* (1976). Inclusion of this run would raise the average value only slightly, to 0.51, but the standard deviation would have increased almost threefold, to $\sigma = 0.28$. The analyzed residual pyroxene in the run in question (A4 of 61SC-A, 1300°C in Table 3) contains very little aluminum (0.3 weight percent Al_2O_3) in relationship to the 0.51 weight percent Cr_2O_3 present in the melt. We suggest that this small content of aluminum in the grain in question, 0.014 Al cations per formula unit, effectively limited the substitution of Cr^{3+} by the coupled substitution $M^{+2}Cr^{+3}Al^{IV}SiO_6$, thereby diminishing the ability of the augite to accept chrommium.

Manganese is not strongly partitioned between pyroxene and liquid, or between individual pyroxenes (Fig. 13d). Fourteen values of $1/D_{Mn}$ range from 0.8 to 2.9 and average 1.5 ($\sigma = 0.7$, $\bar{\sigma} = 0.2$). Three additional values of 1/D were excluded from the averaged data set: they are 1.4 for the suspect run at 1126°C, an anomalous value of 4.7 at 1208°C, and a value at 1123°C of 9.0 for augite that was not in direct contact with the analyzed glass. The four values for $1/D_{Mn}$ of ferrobustamite are similar and average 0.6, distinctly different from the average of the pyroxenes.

In summary, we see that of the four minor components considered only Al_2O_3 and TiO_2 have potential for reaching significantly greater concentration levels in the partial melt than in the crystalline pyroxene. In each of the runs reported in Table 3 the sum of $Al_2O_3 + TiO_2$ exceeds 5 percent oxides by weight (which corresponds to approximately 10 mole percent metasilicate components). Thus Al_2O_3 and, where present, TiO_2 dilute the melt, relative to the pyroxene, in the components that are present in the synthetic system, $CaSiO_3$, $MgSiO_3$, and $FeSiO_3$. As dilution of the melt will lower the activities of $CaSiO_3$, $MgSiO_3$, and $FeSiO_3$ in the melt, we would expect the melting point to be lowered in the natural pyroxene system (Lewis and Randall, 1961, p. 235, 416). The solidus in our natural system is approximately 100°C below the temperature of the solidus in the synthetic system (Fig. 12). Because for every point on the solidus there is an associated liquid at the same temperature, the liquidus surface must be correspondingly lowered in temperature.

IV. Comparison with other systems

Most experimental studies that report analyses of pyroxenes and the melts with which they are (thought to be) in equilibrium pertain to the compositions of lunar basalts and their residual liquids. We will compare our experimental results with research on low-pressure systems drawn from the lunar literature and summarized in Table 4. The examples were selected to show liquids that coexist with each of the pyroxenes and, as far as was practical, to involve liquids with a silica content approximating that of pyroxene partial melts. We specifically compared the tie-lines connecting the compositions of the liquid and pyroxene, projected onto the pyroxene quadrilateral. We also compared the partitioning of minor elements between crystals and melt. We are not disturbed by the fact that the temperatures predicted from our pyroxene phase diagrams do not always correspond with the temperatures reported for similar crystal–liquid assemblages by other investigators. We used pyroxene bulk compositions, and the other authors used whole-rock compositions; the whole-rock compositions, being more dilute in pyroxene components, are expected to have lower ranges of solidus temperatures. Overall, we found that differences in bulk composition and temperature did not greatly affect the partitioning of an element.

Five teams of investigators presented results that conform well with the present study (Table 4). Four of these reports contain microprobe data for the four minor elements that we considered. As a group, these studies encompass a wide range of liquid compositions, including both high- and low-titanium mare basalts, a residual liquid composition, and a model composition for a primitive lunar magma. Data for both pigeonite and augite are available. Such a wide range of bulk compositions yielding data similar to ours suggests that, to a first approximation at least, changes in bulk composition do not change the partitioning of Ca, Mg, Fe, Al, Ti, Cr, and Mn between pyroxenes and liquid.

Representative data for melt coexisting with pigeonite (Walker *et al.,* 1976), orthopyroxene (Longhi, personal communication, 1978), and augite (Biggar *et al.,* 1971) are summarized in greater detail than in Table 4 by compositional projection onto the pyroxene quadrilateral (Fig. 14) and by comparing average bulk partition coefficients (Table 5). Tie-line orientations for the major components and minor-element bulk distribution coefficients predicted from the results of this study are included. Agreement with the results of others appears satisfactory: the slopes of the LP and LA tie lines compare well, and observed ranges of the minor-element distribution coefficients overlap. The apparent discrepancy in the value of $1/D_{Cr}$ for augite (Biggar *et al.*, 1971; 12064 composition at 1114°C) can be attributed to possible analytical error (the "Cr_2O_3" content of their melt is only 0.15 percent by weight) or to the relatively short run time that they used (5 hours).

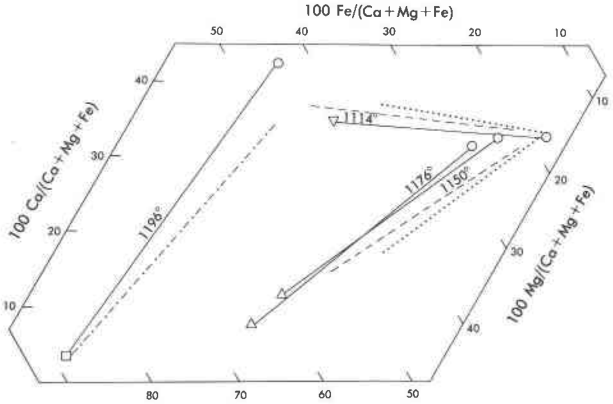

Fig. 14. Comparison of the results of the present investigation with representative results from the literature (summarized in Table 4). Orthopyroxene–liquid, 1196°C (Longhi, personal communication, 1978); pigeonite–liquid, 1150° and 1176°C (Walker *et al.*, 1976); and augite–liquid, 1114°C (Biggar *et al.*, 1971). Tie-lines from this study are as follows: dotted, 1140°C; dashed, 1180°C; dot–dash, 1300°C.

Four reports of isothermal, partial crystallization experiments contain significant discrepancies from our results in both major and minor elements. The four reports will be considered on a case-to-case basis

Table 5. Representative partitioning data

Author	Assemblage	Comp	T°C	1/D Al	1/D Ti	1/D Cr	1/D Mn
Walker et al. (1976)	LP	12002	1176	9.6	6.8	0.6	
	LP	12002	1150	4.9	4.5	0.4	1.0
Present results average value (σ)				13(5.5)	7.4(4.0)	0.45(0.11)	1.5(0.7)
Biggar et al. (1971)	LA	12064	1114	3.2	3.5	0.16	1.0
Present results average value (σ)				7.4(2.1)	4.9(1.5)	0.45(0.11)	1.5(0.7)
Longhi (personal communication, 1978)	LO			7.3	6.0	--	--
Present results average value (σ)				9.9(5.4)	8.1(3.1)		

in an effort to show which sets of results might be valid (and thus serve to establish the limits of uncertainty for such work) and which results appear internally or externally inconsistent (and thus cannot be used to establish uncertainty limits).

In their investigation of Ti and Al partitioning, Akella and Boyd (1973) prepared a glass of pyroxene bulk composition ($Wo_{25}En_{30}Fs_{45}$) to which they added first 10 mole percent $CaTiAl_2O_6$ component, then 2 weight percent SiO_2. The augite and melt from runs made (in iron capsules) at 1160°, 1130°, and 1110°C were analyzed by electron microprobe. Values of $1/D_{Al}$ and $1/D_{Ti}$ for augite agree with those of other investigators (all of whom found slightly less marked partitioning than did we). However, the tie-lines connecting augite and melt in quadrilateral (Ca,Fe,Mg) projection are unusually long, are of dissimilar slope, and the tie-line at 1160°C is parallel to the Di–Hd join. Even though augite and olivine are the only crystalline ferromagnesian phases present, the Fe/(Mg + Fe) ratios of the augite and the melt do not change with decreasing temperature (increase in amount of crystals). The results appear to be internally inconsistent.

O'Hara *et al.* (1974) reported analyses of crystals and melts produced by isothermal equilibration of three high-titanium lunar basalts (10017 at 1108°, 10020 at 1133°, and 10062 at 1120°C) in molybdenum capsules at an oxygen fugacity close to that of the iron–wüstite equilibrium. Although the bulk compositions of the three experiments are similar, we find that in the first run (1108°C) the augite + liquid tie-line is nearly horizontal; in the second run (1133°C) the liquid is more calcic than the augite: and only in the third run (1120°C) is the liquid less calcic than the augite (the result we anticipated from our own work). In this third run the values of $1/D_{Al}$ and $1/D_{Ti}$ are anomalously small by any standards (Al and Ti are not strongly partitioned between crystals and melt). $1/D_{Cr_2}$ is much larger than expected in the first and third runs (1108° and 1120°C). The only run in which the minor-element data appear reasonable is the second (1133°C), in which the augite has unusually little Wo component (PA tie-line too short). Rather than incorporate those data which agree with ours, and ignore those which don't, we have chosen to ignore entirely all three experimental runs because of the apparent inconsistencies.

Weill and McKay (1975a,b) studied the crystallization of two model lunar compositions. The first report (1975a) presents data on an average lunar highlands (aluminous) basalt and indicates that $1/D_{Al}$ for pyroxene is slightly smaller than the value we found. In addition, the Fe/(Mg + Fe) of the coexisting melt is unexpectedly large for pyroxene with the Fe/(Mg + Fe) observed by Weill and McKay. (Compare this result with that of Longhi, 1978.) We cannot attribute the discrepancies to the aluminous nature of the bulk composition because at 1200°, the temperature of pyroxene crystallization, the melt resembles that of a magnesian mare basalt (13.6 percent Al_2O_3 by weight). We have no good explanation for the discrepancy, but do note that at somewhat higher temperatures the change in melt composition was not complementary to the compositions of the solids reported to precipitate—an internal inconsistency. A subsequent investigation by Weill and McKay (1975b) involved a model "ferromagnesian" composition with a much smaller initial anorthite component. However, plagioclase did not precipitate, and this allowed the Al_2O_3 and CaO content of the melt to rise. The minor-element partitioning between melt and orthopyroxene agrees with our own data, but again the melt has a surprisingly large Fe/(Fe + Mg) for such magnesian orthopyroxene. Furthermore, we are surprised at the large buildup in the Al_2O_3 content of the orthopyroxene as temperature decreased; 5 percent by weight is unusually large for equilibrium precipitation at 1 bar. Although our results agree with most of the minor-element data, we don't think we should incorporate them in our work if we have reservations about the major-element partitioning.

In summary, six sets of data, including our own results, agree with respect to tie-line orientation in Ca–Fe–Mg projection. This tie-line orientation appears sensitive to the proportions of Ca, Fe, and Mg, but relatively indifferent to temperature or bulk composition. We suggest that our diagrams can be used to predict the partitioning of Ca, Fe, and Mg between pyroxenes and melt for liquids of basaltic composition, and perhaps a much wider range of liquids. The minor-element data must be used with greater caution (Table 5). Our average values (1/D) for Al and Ti in calcium-poor pyroxene (11 and 7.8, respectively) are slightly larger than the average of the values of other investigators (7.3 and 6.4). Our values for Al and Ti in augite are consistently greater than the values of other investigators; we found 7.4 and 4.9 and their values average 3.4 and 3.8, respectively. It is tempting to regard the results of our partial melting experiments and those of partial crystallization experiments by other investigators as values reversing or bracketing an equilibrium, then assume that the mean value is the "equilibrium" value. These averaged values for (1/D) in Al and Ti would then be 9.2 and 7.5 in pigeonite and orthopyroxene, 5.4 and 4.4 in augite. Our values of 1/D for Cr and Mn in pyroxene, 0.45 and 1.5, respectively, are in fair agreement with the average of previous determinations: 0.32 and 0.83 in pigeonite, and 0.17 and 0.93 in augite. Most of the discrepancies between our results and those of previous investigators involve runs in which the major-element partitioning appears inconsistent when compared with runs of similar composition reported by the same investigators.

Minor elements and equilibrium

Recent kinetic studies have permitted evaluation of the effects that a departure from equilibrium has on the texture (Lofgren *et al.*, 1974), on the crystallization sequence (Grove and Raudsepp, 1978), and on the temperature of crystallization (Walker *et al.*, 1976). In an experimental study of pyroxene–liquid interaction on crystallization, Grove and Bence (1977) found that the partitioning of major elements, (CaO, MgO, FeO) is nearly independent of cooling rate. In contrast, bulk distribution coefficients (D) for Al_2O_3 and TiO_2 varied in such manner that the faster the cooling rate, the greater the concentration of these minor elements in the pyroxene that is crystallizing (and thus the smaller the degree of fractionation between crystals and liquids). Because melt is converted to pyroxene having a lower concentration of Al and Ti, these elements are concentrated about the margin of the growing pyroxene crystal. Under rapid cooling rates, the Al and Ti do not have a chance to diffuse away from the growing crystal and the pyroxene rims will have anomalously large concentrations of Al_2O_3 and TiO_2. At best, only local equilibrium is achieved.

Although we realize that in detail the mechanics of the melting process are not the same as those of crystallization, we suggest that the degree of minor-element partitioning could be an indicator of disequilibrium. For partial melting experiments, our values of both the minor- and major-element distribution coefficients are similar to those measured in experiments in which pyroxene crystallized from melt (heated glass) at constant temperature. These experiments would constitute a reversal of our experiments but for the differences in bulk composition, especially the concentrations of CaO, MgO, FeO, and SiO_2. In other experiments, the devitrification products of a glass (melt) are annealed at constant temperature, approaching the same final state by a different path. The agreement in the minor-element partitioning constants, determined by the different sets of experiments, indeed suggests that equilibrium has been approached in each kind of experiment.

V. Application to petrologic problems

The phase diagrams presented in this paper should prove useful to petrologists, in the field and in the laboratory. These diagrams should help the experimentalist to select combinations of temperature and composition for laboratory experiments involving pyroxene crystals and melts. For example, much time can be saved in a study of the trace-element distribution between augite and melt if one knows in advance the temperature at which equal proportions of crystals and melt are present. Or in the measurement of the electrical conductivity of a tediously characterized, oriented, cut, and polished plate of orthopyroxene, it is useful to know the maximum temperature to which the plate can be heated without melting. The diagrams may also prove useful for judging whether or not equilibrium was obtained in partial melting or crystallization experiments at one bar. These diagrams will not be as useful in explaining the partial melting or crystallization relations of rocks until the effects of changing silica content (and other variables) are understood. Nevertheless, the diagrams should indicate the compositional trends of both crystals and solids as fractional melting or crystallization proceeds.

Pyroxene crystallization trends in gabbroic rocks

Modern petrology texts (see, for instance, Carmichael *et al.*, 1974) discuss the pyroxene crystallization trends summarized by Hess (1941). Many data on these trends in gabbroic and basaltic rocks have been accumulated in the intervening years, and the importance of the silica activity to pyroxene and olivine crystallization has been discussed (Lindsley and Munoz, 1969). However, the compositional data necessary to define the liquidus boundaries for pyroxenes in basalts are, surprisingly, not yet available. In lieu of accurate data on the compositions of pyroxenes and the melts from which they crystallized, we must explain the pyroxene crystallization trends using phase diagrams for pyroxene bulk compositions as substitutes for gabbroic compositions. We will use the diagrams for natural pyroxene bulk compositions (Fig. 10), because this approach will be far more successful than using phase diagrams for either the bounding binary and ternary systems (Fig. 2) or the synthetic system CaO–MgO–FeO–SiO_2 discussed earlier.

Alkali–olivine basalt

A single pyroxene, calcic augite, crystallizes from alkali–olivine basalt magma. The trend of augite composition in rocks of this bulk composition lies approximately parallel to the Di–Hd join; Fe/(Mg + Fe) increases with progressive crystallization as the clinopyroxene being precipitated changes from approximately $Wo_{48}En_{40}Fs_{12}$ to $Wo_{46}En_{31}Fs_{23}$ (Wilkinson, 1956; Elsdon, 1971). The pyroxene trend is a clue to the compositional evolution of the melt during fractional crystallization. The augite trend, coupled with knowledge of the orientation of the augite + liquid tie-lines, indicates that for a wide range of Fe/(Mg + Fe) the liquid is richer in iron, and only slightly poorer in calcium component, than the coexisting augite. The residual melt must evolve toward more iron-rich compositions, following a path that is nearly parallel to the boundary curve L(P,A). Our diagrams indicate that precipitation of augite is not likely to force the liquid to the field of calcium-poor pyroxene. This supposition is confirmed by actual alkali–olivine basalts, which typically are devoid of orthopyroxene or pigeonite, and by the existence of the thermal divide olivine–augite–plagioclase, at least in the iron-free system (Presnall *et al.*, 1978). It must be emphasized that the pyroxenes alone do not exclusively control the compositional evolution of the residual alkali–olivine basalt melt, but they do record its evolution. Olivine and plagioclase commonly crystallize in equilibrium with the augite; spinel does so less commonly. We suspect that the melt evolves along or close to a univariant curve liquid + calcium-poor pyroxene + augite + olivine + plagioclase ± magnetite, which we postulate to be subparallel to the Di–Hd join at a silica content between the pyroxene and olivine planes.

Tholeiitic basalt

The compositional trend of pyroxenes that crystallize from tholeiitic magmas is considerably more complicated than the simple trend just discussed. Augite crystallizes in equilibrium with calcium-poor pyroxene, initially an orthopyroxene, later pigeonite. With progressive crystallization, the Fe/(Mg + Fe) of the pyroxenes increases. This trend is known in both intrusive rocks (*i.e.* the Bushveld Complex; Atkins, 1969) and extrusives (*i.e.*, a Hakone andesite; Nakamura and Kushiro, 1970). Olivine crystallization commonly accompanies pyroxene during the early and late stages of crystallization, but is absent in the intermediate stages (*i.e.*, Wager and Brown, 1967; Wright and Weiblen, 1967).

The trend of the tholeiite melt phase, projected onto the pyroxene quadrilateral, can be described as following the boundary between augite and calcium-poor pyroxene during the early and intermediate stages of crystallization, then moving into the augite field during the late stage. If we assume that plagioclase (Pc) and perhaps magnetite (Mt) crystallize with the pyroxene, the assemblages are L(O,A,F,Pc, ±Mt), L(A,P,Pc, ±Mt), and L(A,F,Pc,±Mt). The fact that the melt leaves the two-pyroxene boundary between augite and pigeonite and precipitates augite indicates that fractional crystallization of augite alone does not control the evolution of the residual liquid. Clearly, crystallization of a calcium-poor phase such as olivine is necessary to cause the augite and the liquid to become more calcic.

The disappearance and reappearance of olivine can be explained in terms of the silica activity of the melt and the stability of Ca-poor pyroxene (Lindsley and Munoz, 1969). An alternative way of looking at the problem is to construct the liquidus boundary surfaces in a polycomponent liquidus diagram. Thus, we can speak of a liquid path that follows a curve or moves across a surface. In the tholeiite magma, the melt follows the curve L(O,A,F) that pierces the pyroxene quadrilateral liquidus (Fig. 9a), moves along the L(O,A) and/or L(P,A) surfaces that separate the augite and Ca-poor pyroxene volumes, and then moves across the surface that separates the augite and olivine fields.

Future work

We recognize that the preceding discussion of basalt crystallization is extremely qualitative. Two kinds of data will be necessary before the fractional crystallization of basaltic magma can be understood in terms of the temperature–composition space presented in our diagrams. First, we need more experimental data, including the kind presented here, obtained for bulk compositions that lie between the olivine and pyroxene planes. During our partial melting experiments, a number of our charges gained iron (as FeO), moving the bulk composition toward FeO and hence toward the olivine plane (Fig. 1). One of us (JSH) is now assembling the data on these runs in order to learn the positions of the univariant curves which pierce the pyroxene quadrilateral plane, and to locate the liquidus surfaces which bound the olivine volume. A second kind of data, analyses of phenocrysts and the residual basaltic liquids with which they are in equilibrium, is surprisingly scarce. We hope that other workers will soon generate such data and test the effectiveness of our diagrams in understanding and predicting the crystallization and partial melting of basalts.

Acknowledgments

In addition to the institutions with which the authors are associated, support for this research effort was provided by the NASA Lunar Sample Progam (Contract T-2356A to Huebner) and by the National Research Council of Canada (Grant NSERC A2688 to Turnock). Several individuals significantly advanced the progress of this investigation. D. J. Putt assisted Turnock with some of the experiments on synthetic compositions. Nelson L. Hickling assisted Huebner in obtaining microprobe data in 1973; Mary Woodruff helped reduce those data to obtain analyses. Lovell B. Wiggins maintained the microprobe in excellent condition and operated the automated instrument to collect the analyses dated 1976. Malcom Ross of the U.S. Geological Survey kindly obtained the cell dimensions of the pyroxenoid, confirming its identity as ferrobustamite. Donald Lindsley of SUNY–Stony Brook discussed the results with us as the study progressed. E-an Zen and Edwin Roedder of the U.S. Geological Survey provided thorough reviews that helped us improve greatly the clarity of our presentation; Neil Irvine, Donald Lindsley, John Longhi, and David Walker constructively reviewed a subsequent version of the manuscript.

References

Akella, J. and F. R. Boyd (1973) Partitioning of Ti and Al between coexisting silicates, oxides, and liquids. *Proc. Lunar Sci. Conf. 4th,* 1049–1059.

Atkins, F. B. (1969) Pyroxenes of the Bushveld Intrusion, South Africa. *J. Petrol., 10,* 222–249.

Biggar, G. M. and D. B. Clarke (1971) Aspects of phase equilibria in the inversion and exsolution of pyroxene. *Indian Mineral., 12,* 1–13.

———, M. J. O'Hara, A. Peckett and D. J. Humphries (1971) Lunar lavas and the achondrites: petrogenesis of protohypersthene basalts in the maria lava lakes. *Proc. Lunar Sci. Conf. 2nd,* 617–643.

Bonnichsen, B. (1969) Metamorphic pyroxenes and amphiboles in the Biwabik Iron formation, Dunka River area, Minnesota. *Mineral Soc. Am. Spec. Pap., 2,* 217–239.

Bowen, N. L. and J. F. Schairer (1935) The system MgO–FeO–SiO$_2$. *Am. J. Sci., 29,* 151–217.

———, ——— and E. Posnjak (1933) The system CaO–FeO–SiO$_2$. *Am. J. Sci., 26,* 193–284.

Boyd, F. R. and J. F. Schairer (1964) The system MgSiO$_3$–CaMgSi$_2$O$_6$. *J. Petrol., 5,* 275–309.

——— and D. Smith (1971) Compositional zoning in pyroxenes from lunar rock 12021, Oceanus Procellarum. *J. Petrol., 12,* 439–464.

Brown, G. M. and E. A. Vincent (1963) Pyroxenes from the late stages of fractionation of the Skaergaard Intrusion, East Greenland. *J. Petrol., 4,* 175–97.

Carmichael, I. S. E., F. J. Turner and J. Verhoogen (1974) *Igneous Petrology.* McGraw-Hill, New York.

Coleman, R. G. and J. R. Clark (1968) Pyroxenes in the blueschist facies of California. *Am. J. Sci., 266,* 43–59.

Crawford, M. L. (1966) Optical properties of metamorphic albite. *Am. Mineral., 51,* 523–524.

Dallwitz, W. B., D. H. Green and J. E. Thompson (1966) Clinoenstatite in a volcanic rock from the Cape Vogel area, Papua. *J. Petrol., 7,* 375–403.

Desborough, G. A. and H. J. Rose, Jr. (1968) X-ray and chemical analysis of orthopyroxenes from the lower part of the Bushveld complex, South Africa, *U.S. Geol. Surv. Prof. Pap., 600-B,* B1–B5.

Elsdon, R. (1971) Clinopyroxenes from the Upper Layered Series, Kap Edvard Holm, East Greenland. *Mineral Mag., 38,* 49–57.

Foster, W. R. and H. C. Lin (1975) New data on the forsterite–diopside–silica system (abstr.) *Trans. Am. Geophys. Union, 56,* 470.

Grove, T. L. and A. E. Bence (1977) Experimental study of pyroxene–liquid interaction in quartz-normative basalt 15597. *Proc. Lunar Sci. Conf. 8th,* 1549–1579.

——— and M. Raudsepp (1978) Effects of kinetics on the crystallization of quartz normative basalt 15597: an experimental study. *Proc. Lunar Planet. Sci. Conf. 9th,* 585–599.

Grover, J. (1972) The stability of low-clinoenstatite in the system Mg$_2$Si$_2$O$_6$–CaMgSi$_2$O$_6$, (abstr.). *Trans. Am. Geophys. Union, 53,* 539.

———, D. H. Lindsley and A. C. Turnock (1972) Ca–Mg–Fe pyroxenes: subsolidus phase relations in iron-rich portions of the pyroxene quadrilateral. *Geol. Soc. Am. Abstracts with Programs, 4,* 521–522.

Heald, E. F. (1967) Thermodynamics of iron–platinum alloys. *Trans. Met. Soc. AIME, 239,* 1337–1340.

Hess, H. H. (1941) Pyroxenes of common mafic magmas. Part 1. *Am. Mineral., 26,* 515–535.

Huebner, J. S. (1973) Experimental control of wüstite activity and mole fraction (abstr.). *Geol. Soc. Am. Abstracts with Programs, 5,* 676–677.

——— (1975) Origin of the SiO$_2$ variation of mare basalt melts. *Lunar Sci. VI,* p. 411–413. Lunar Science Institute, Houston, Texas.

——— and M. Ross (1972) Phase relations of lunar and terrestrial pyroxenes at one atmosphere. *Lunar Sci. III,* p. 410–412. Lunar Science Institute, Houston, Texas.

———, B. R. Lipin and L. B. Wiggins (1976) Partitioning of chromium between silicate crystals and melt. *Proc. Lunar Sci. Conf. 7th,* 1195–1220.

———, M. Ross, N. Hickling and A. C. Turnock (1972) Partial melting of pyroxenes and the origin of mare basalts. *Lunar Sci. IV,* p. 397–399. Lunar Science Institute, Houston, Texas.

Jaffe, H. W., P. Robinson, R. J. Tracy and M. Ross (1975) Orientation of pigeonite exsolution lamellae in metamorphic augite: correlation with composition and calculated optimal phase boundaries. *Am. Mineral., 60,* 9–29.

Jarosewich, E., A. S. Parker and L. B. Wiggins (1979) Microprobe analyses of four natural glasses and one mineral—an interlaboratory study of precision and accuracy. *Smithsonian Contrib. Earth Sci., 22,* 53–67.

Kuno, H. (1966) Review of pyroxene relations in terrestrial rocks in the light of recent experimental works. *Mineral. J., 5,* 21–43.

Kushiro, I. (1972) Determination of liquidus relations in synthetic silicate systems with electron probe analysis: the system forsterite–diopside–silica at 1 atmosphere. *Am. Mineral., 57,* 1260–1271.

Lewis, G. N. and M. Randall (revised by K. S. Pitzer and L. Brewer) (1961) *Thermodynamics.* McGraw-Hill, New York.

Lindsley, D. H. and J. L. Munoz (1969) Subsolidus relations along the join hedenbergite–ferrosilite. *Am. J. Sci., Schairer Volume, 267-A,* 295–324.

Lofgren, G., C. H. Donaldson, R. J. Williams, O. Mullins, Jr. and T. M. Usselman (1974) Experimentally reproduced textures and mineral chemistry of Apollo 15 quartz normative basalts. *Proc. Lunar Sci. Conf. 5th,* 549–567.

Longhi, J. (1978) Pyroxene stability and the composition of the lunar magma ocean. *Proc. Lunar Sci. Conf. 9th,* 285–306.

——— and A. E. Boudreau (1979) Pyroxene liquidus fields in basaltic liquids at low pressure. *Lunar and Planetary Science X,* p. 739–741. Lunar and Planetary Science Institute, Houston, Texas.

———, D. Walker, T. L. Grove, E. M. Stolper and J. F. Hays (1974) The petrology of the Apollo 17 mare basalts. *Proc. Lunar Sci. Conf. 5th,* 447–469.

Mason, B. and R. O. Allen (1972) Minor and trace elements in augite, hornblende, and pyrope megacrysts from Kakanui, New Zealand, *N.Z. J. Geol. Geophys., 16,* 935–947.

Minkin, J. A., E. C. T. Chao, R. P. Christian, E. E. Harris and D. R. Norton (1976) Three synthetic lunar glasses. *Meteoritics, 11,* 167–171.

Nafziger, R. H., G. C. Ulmer and E. Woermann (1971) Gaseous buffering for the control of oxygen fugacity at one atmosphere. In G. C. Ulmer, Ed., *Research Techniques for High Pressure and High Temperature,* p. 9–42. Springer-Verlag, New York.

Nakamura, Y. (1971) Equilibrium relations in Mg-rich part of the pyroxene quadrilateral. *Mineral. J., 6,* 264–276.

——— and I. Kushiro (1970) Equilibrium relations of hypersthene, pigeonite and augite in crystallizing magmas: microprobe study of a pigeonite andesite from Weiselberg, Germany. *Am. Mineral., 55,* 1999–2015.

Nolan, J. (1969) Physical properties of synthetic and natural pyroxenes in the system diopside–hedenbergite–acmite. *Mineral. Mag., 37,* 216–229.

O'Hara, M. J., G. M. Biggar, P. G. Hill, B. Jefferies and D. J. Humphries (1974) Plagioclase saturation in lunar high-titanium basalt. *Earth Planet. Sci. Lett., 21,* 253–268.

Presnall, D. C., S. A. Dixon, J. R. Dixon, T. H. O'Donnell, N. L. Brenner, R. L. Schrock and D. W. Dycus (1978) Liquidus phase relations on the join diopside–forsterite–anorthite from 1 atm to 20 kbar; their bearing on the generation and crystallization of basaltic magma. *Contrib. Mineral. Petrol., 66,* 203–220.

Prewitt, C. T., G. E. Brown and J. J. Papike (1971) Apollo 12 clinopyroxenes: high temperature X-ray diffraction studies. *Proc. Lunar Sci. Conf. 2nd,* 59–68.

Prince, A. (1966) *Alloy Phase Equilibria.* Elsevier Publishing Company, New York.

Rapoport, P. A. and C. W. Burnham (1973) Ferrobustamite: the crystal structures of two Ca,Fe bustamite-type pyroxenoids. *Z. Kristallogr., 138,* 419–438.

Roedder, E. (1965) A laboratory reconnaissance of the liquidus surface in the pyroxene system En–Di–Hd–Fs ($MgSiO_3$–$CaMgSi_2O_6$–$CaFeSi_2O_6$–$FeSiO_3$). *Am. Mineral., 50,* 696–703.

Ross, M. and J. S. Huebner (1975) A pyroxene geothermometer based on composition–temperature relationships of naturally occurring orthopyroxene, pigeonite, and augite. *Extended Abstracts, Int. Conf. Geothermometry and Geobarometry.* Pennsylvania State University, University Park, Pennsylvania.

——— and ——— (1979) Temperature–composition relationships between naturally occurring augite, pigeonite, and orthopyroxene at one bar pressure. *Am. Mineral., 64,* 1133–1155.

———, ——— and E. Dowty (1973) Delineation of the one atmosphere augite–pigeonite miscibility gap for pyroxenes from lunar basalt 12021. *Am. Mineral., 58,* 619–635.

———, ——— and N. L. Hickling (1972) Delineation of the orthopyroxene–pigeonite transition and its bearing on pyroxene phase relations in lunar rocks (abstr.). *Lunar Sci. IV,* p. 637–639. Lunar Science Institute, Houston, Texas.

Rutstein, M. and R. A. Yund (1969) Unit-cell parameters of synthetic diopside–hedenbergite solid solutions. *Am. Mineral., 54,* 238–245.

Schwab, R. G. (1969) Die Phasenbeziehungen im System $CaMgSi_2O_6$–$CaFeSi_2O_6$–$MgSiO_3$–$FeSiO_3$. *Fortschr. Mineral., 46,* 188–273.

Simmons, E. C., D. H. Lindsley and J. J. Papike (1974) Phase relations and crystallization sequence in a contact-metamorphosed rock from the Gunflint Iron Formation, Minnesota. *J. Petrol., 15,* 539–65.

Smith, D. (1971) Stability of the assemblage iron-rich orthopyroxene–olivine–quartz. *Am. J. Sci., 271,* 370–382.

Smith, J. V. (1969) Crystal structure and stability of the $MgSiO_3$ polymorphs; physical properties and phase relations of Mg,Fe pyroxenes. *Mineral. Soc. Am. Spec. Pap., 2,* 3–29.

Turnock, A. C. (1962) Preliminary results on melting relations of synthetic pyroxenes on the diopside–hedenbergite join. *Carnegie Inst. Wash. Year Book, 61,* 82.

——— (1970) Phase relations of synthetic Mg–Fe–Ca pyroxenes. *Am. Mineral., 55,* 314.

———, D. H. Lindsley and J. E. Grover (1973) The synthesis and unit cell parameters of Ca–Mg–Fe pyroxenes. *Am. Mineral., 58,* 50–59.

Wager, L. R. and G. M. Brown (1967) *Layered Igneous Rocks.* Freeman, San Francisco, California.

——— and W. A. Deer (1939) Geological investigations in East Greenland. Part III. The petrology of the Skaergaard Intrusion, Kangerdlugssuaq, East Greenland. *Meddelelser om Grønland, 105,* 1–352.

Walker, D., R. J. Kirkpatrick, J. Longhi and J. F. Hays (1976) Crystallization history and origin of lunar picritic basalt 12002: phase equilibria, cooling rate studies, and physical properties of the parent magma. *Bull. Geol. Soc. Am., 87,* 646–656.

Weill, D. F. and G. A. McKay (1975a) Major and trace element trends during minor experiments on the crystallization of lunar melts. *Lunar Sci. VI,* p. 863–865. Lunar Science Institute Houston, Texas.

——— and ——— (1975b) The partitioning of Mg,Fe,Sr,Ca,Sm,Eu, and Yb in lunar igneous systems and a possible origin of KREEP by equilibrium partial melting. *Proc. Lunar Sci. Conf. 6th,* 1143–1158.

Wilkinson, J. F. G. (1956) Clinopyroxenes of alkali olivine-basalt magma. *Am. Mineral., 41,* 724–743.

Williams, R. J. (1971) Reaction constants in the system Fe–Mg–SiO_2–O_2 at 1 atm between 900° and 1300°C: experimental results. *Am. J. Sci., 270,* 334–360.

Wright, T. L. and P. W. Weiblen (1967) Mineral composition and paragenesis in tholeiitic basalt from Makaopuhi Lava Lake, Hawaii. *Geol. Soc. Am. Abstracts with Programs,* 242–243.

Yang, H. Y. (1973) Crystallization of iron-free pigeonite in the system anorthite–diopside–enstatite–silica at atmospheric pressure. *Am. J. Sci.*, *273*, 488–497.

——— and W. R. Foster (1972) Stability of iron-free pigeonite at atmospheric pressure. *Am. Mineral.*, *57*, 1232–1241.

Yoder, H. S., Jr. and Th. G. Sahama (1957) Olivine X-ray determinative curve. *Am. Mineral.*, *42*, 475–491.

———, C. E. Tilley and J. F. Schairer (1963) Pyroxenes and associated minerals in the crust and mantle. *Carnegie Inst. Wash. Year Book*, *62*, 84–95.

———, ——— and ——— (1964) Isothermal sections of pyroxene quadrilateral. *Carnegie Inst. Wash. Year Book*, *63*, 121–129.

Manuscript received, April 16, 1979;
accepted for publication, October 15, 1979.